



Title	Synthesis and Characterizations of Vertical Ferromagnetic MnAs/Semiconducting InAs Heterojunction Nanowires
Author(s)	小平, 竜太郎
Citation	北海道大学. 博士(工学) 甲第13514号
Issue Date	2019-03-25
DOI	10.14943/doctoral.k13514
Doc URL	http://hdl.handle.net/2115/74180
Type	theses (doctoral)
File Information	Ryutaro_Kodaira.pdf



[Instructions for use](#)

Doctoral Dissertation

博士論文

Synthesis and Characterizations of Vertical Ferromagnetic
MnAs/Semiconducting InAs Heterojunction Nanowires

(強磁性体 MnAs/半導体 InAs 縦型ヘテロ接合ナノワイヤの成長と評価に関する研究)

Graduate School of Information Science and Technology,
Hokkaido University

北海道大学大学院情報科学研究科

Ryutaro Kodaira

小平 竜太郎



© 2019 Ryutaro Kodaira

A dissertation submitted in partial fulfillment
of the requirements for the degree of Doctor of
Philosophy (Engineering)
in Hokkaido University, February 2019.

Dissertation Supervisor
Associate Professor Shinjiro Hara

Acknowledgements

This dissertation describes a part of research work carried out at Research Center for Integrated Quantum Electronics (RCIQE), Hokkaido University, under the supervision of Prof. Shinjiro Hara, while I was graduate student at the Graduate School of Information Science Technology, Hokkaido University.

I especially wish to express my sincere appreciation to Supervisor, Prof. Shinjiro Hara. This work would never be accomplished without his invaluable support, guidance, and encouragement. I am greatly happy to study and research for six years under his supervision.

I would like to express my sincere thanks to Prof. Junichi Motohisa and Prof. Tamotsu Hashizume for their continual support and insightful comments.

I would like to express my gratitude to Prof. Yasuo Takahashi for the illuminating and productive discussions I had with him.

I would like to express my appreciation to Prof. Eiichi Sano, Prof. Kanji Yoh, Prof. Seiya Kasai, Prof. Masayuki Ikebe, Prof. Masamichi Akazawa, Prof. Taketomo Sato, Prof. Katsuhiko Tomioka, and Prof. Takashi Fukui for their encouragement and fruitful discussions.

I would like to say thanks to the member of our research group, Dr. Keitaro Ikejiri, Dr. Yoshinori Kohashi, Dr. Eiji Nakai, Mr. Masatoshi Yatago, Dr. Shinya Sakita, Mr. Hiromu Fujimagari, Mr. Shogo Yanase, Mr. Hiroaki Kato, Mr. Toshihiro Wada, Mr. Muye Chen, Mr. Yoshihiro Hiraya, Mr. Hiroki Kameda, Mr. Kyohei Kabamoto, Mr. Akinobu Yoshida, Mr. Kohei Chiba, Mr. Ryoma Horiguchi, Mr. Masahiro Sasaki, Mr. Yusuke Minami, Mr. Tetsuro Kadowaki, Mr. Masaya Iida, Mr. Yuki Kitazawa, Mr. Kozaburo Suzuki, Mr. Tomoya Akamatsu, Mr. Hironori Gamou, Mr. Keigo Teramoto, for their technical supports, valuable discussions and encouragement.

I wish to say thanks for RCIQE researchers and students, Dr. Zenji Yatabe, Dr. Joel T. Asubar, Dr. Maciek Matys, Dr. Taketsugu Ishikura, Dr. Zhixin Cui, Dr. Masaki Sato, Dr. Xiang Yin, Dr.

Yusuke Kumazaki, Mr. Takuma Nakano, Dr. Ryota Kuroda, Mr. Yushi Abe, Mr. Shinya Inoue, Mr. Yutaka Senzaki, Mr. Takao Miyamoto, Mr. Akio Watanabe, Mr. Masahito Chiba, Dr. Kenya Nishiguchi, Mr. Kento Shirata, Mr. Ryo Wakamiya, Mr. Jyoji Ohira, Mr. Takehiro Kawauchi, Mr. Taro Itatsu, Mr. Tomohide Yoshikawa, Mr. Akihito Sonoda, Mr. Yuki Inden, Mr. Masaaki Edamoto, Ms. Sayaka Ohmi, Mr. Shoma Okamoto, Mr. Hirofumi Kida, Mr. Kentaro Sasaki, Mr. Atsushi Seino, Mr. Shun Takayashiki, Mr. Takuya Miyajima, Mr. Yukinori Wakita, Mr. Keisuke Ito, Mr. Kenta Saito, Mr. Satoru Matsumoto, Mr. Shota Kaneki, Mr. Shota Toiya, Mr. Taito Hasezaki, Mr. Dai Hasegawa, Mr. Shota Hiramatsu, Mr. Naoshige Yokota, Mr. Yuji Ando, Mr. Tatsuya Oyobiki, and I also express thank to the all RCIQE students for their friendship.

I would like to extend my deepest gratitude to Mr. Kenji Takada, Mr. Kiyotake Nagakura, Ms. Satoko Takeuchi, Ms. Mizuho Tanaka, Ms. Yuki Watanabe, Ms. Yuka Kamoto, and Ms. Chieko Akiyama for their businesslike supports and encouragements.

I would like to express my sincere thanks to Prof. Peter J. Klar, Dr. Matthias T. Elm, Dr. Martin. Fischer, Dr. Lars Ostheim, Mr. Fabian Alexander, and Mr. Patrick Uredat for invaluable discussions, support, encouragement, and their kind hospitality during my stay in Gießen, Germany. I had a precious time with them, and I really like German food, beer, and culture. I am so thankful to have met them.

Finally, I am particularly grateful to my parents and grandmother, Tomohiro Kodaira, Hitomi Kodaira, and Sumiko Nakano, who have always provided heartfelt support and encouragement. Thank you from the bottom of my heart.

February 2019
Ryutaro Kodaira

Table of Contents

Acknowledgements	i
Contents	iii
List of Figures	vii
List of Tables	xiii

Chapter 1

Introduction	1
1.1 Background	1
1.1.1 Vertical free-standing semiconducting nanowires	1
1.1.2 Hybrid structures between magnetic and semiconducting materials	2
1.2 Objective	4
1.3 Outline of this thesis	5
Bibliography	7

Chapter 2

Semiconducting Nanowires	11
2.1 Introduction	11
2.1.1 History of nanowire growth	11
2.1.2 Advantages of nanowires	12
2.2 Nanowire growth method	13
2.2.1 Catalyst-assisted vapor-liquid-solid growth	13
2.2.2 Selective-area metal-organic vapor phase epitaxy	14
Bibliography	15

Chapter 3

Experimental Techniques	17
3.1 Introduction	17
3.2 Principles of MOVPE	17
3.2.1 Overviews	17
3.2.2 MOVPE growth process	18
3.2.3 MOVPE growth system	19
3.3 Nanowire fabrication by selective-area MOVPE	21
3.4 Lateral nanowire sample fabrication	21
3.5 Characterizations	22
Bibliography	24

Chapter 4

Growth of Ferromagnetic MnAs/Semiconducting InAs Heterojunction Nanowires	25
4.1 Introduction	25
4.2 Experimental procedure	27
4.3 Results and discussion	28
4.3.1 Structural characterizations	28
4.3.2 Growth condition dependences and growth mechanism of MnAs nanoclusters	32
4.4 Conclusions	41
Bibliography	43

Chapter 5

Magnetization Characterization of MnAs Nanoclusters in Heterojunction Nanowires	45
5.1 Introduction	45

5.2 Experimental procedure	46
5.3 Results and discussion	47
5.3.1 Magnetization along a-axes	47
5.3.2 Magnetization along c-axis	49
5.3.3 Magnetization in a bended heterojunction nanowire	51
5.4 Conclusions	58
Bibliography	59

Chapter 6

Magnetotransport Characterization of Single Nanowires	61
6.1 Introduction	61
6.2 Experimental procedure	62
6.3 Results and discussion	63
6.3.1 Magnetotransport properties of single InAs nanowires	63
6.3.2 Magnetotransport properties of single MnAs/InAs nanowires	67
6.4 Conclusions	68
Bibliography	70

Chapter 7

Conclusion	73
-------------------------	-----------

List of Publications/Conferences/Awards	77
--	-----------

List of Figures

Figure 2-1	Number of published papers about NW is plotted as a function of year. Data was obtained from the Web-of-Science database with the following combination of keywords, “topic = nanowire or nanowires”.12
Figure 2-2	Schematic illustration of VLS growth of a Si NW using a Au catalyst. (a) The Au seed particle is deposited on the substrate. (b) Au-Si liquid alloy is formed by heating and supplying Si source materials. (c) Nucleation occurs at the interface between the liquid alloy and the substrate surface, and then NW begins to grow.13
Figure 2-3	Schematic illustration of catalyst-free SA-MOVPE growth. (a) SiO ₂ thin film is deposited on the substrate. (b) Initial circular openings are fabricated in the SiO ₂ thin film by lithography and etching. (c) Nucleation occurs on the substrate surface within the mask opening region, and then NW begins to grow.14
Figure 3-1	Schematic illustration of growth mechanism of SA-MOVPE process.19
Figure 3-2	Schematic illustration of the MOVPE system used in this study. The horizontal reactor is maintained at working pressure of 0.1 atm and with a total flow of 3.00 SLM.20
Figure 3-3	Schematic illustration of the lines of a MO source provided from a bubbler. When the MO source is used, the red (blue) valves are opened (closed).20
Figure 4-1	Bird’s-eye view SEM images of typical (a) host InAs NW array template before the synthesis of MnAs NCs and (b) MnAs/InAs heterojunction NWs. Inset of (a) is a top view SEM image of crystal facets typically formed on top of host InAs NWs.28
Figure 4-2	Cross-sectional TEM images of ferromagnetic MnAs NCs formed (a) in the middle and (b) on the top {111}B crystal facet of semiconducting InAs NWs. MnAs NCs were grown at 580 °C for 1 min. Cross-sectional TEM images with

	corresponding line profile obtained by EDX spectroscopy for (c) middle and (d) top of NW. The percentages of arsenic, indium, and manganese elements were estimated by eliminating possible external contamination by chemicals (or atoms), such as carbon, oxygen, and silicon, which were possibly introduced during sample preparation processes and from materials of sample holders used for TEM observations. (e) Electron-beam diffraction pattern for MnAs NCs showing MnAs NCs with hexagonal NiAs-type crystal structure. (f) Lattice image of atomically abrupt heterointerface between InAs and MnAs layers that were formed in the middle of NW.30
Figure 4-3	(a) Highly magnified cross-sectional TEM image of middle of vertical MnAs/InAs hybrid NWs in which MnAs NCs were grown at 490 °C for 1 min. (b) Lattice image for one of the MnAs NCs formed in the middle of the host InAs NW. Line profiles obtained by EDX spectroscopy for (c) middle and (d) top parts of the MnAs/InAs hybrid NW. The percentages of arsenic, indium, and manganese elements were estimated by eliminating possible external contamination by chemicals (or atoms), such as carbon, oxygen, and silicon.31
Figure 4-4	Bird's-eye view SEM images of (a) the InAs NW templates and (b) the InAs NWs after the H ₂ treatment where we supplied only H ₂ at 490 °C for 1 min immediately after the growth of the InAs NW templates grown at 580 °C for 30 min.34
Figure 4-5	(a) Average height of host InAs NWs and vertical MnAs/InAs heterojunction NWs were estimated using 30 randomly chosen NWs observed in SEM images. They are plotted as a function of the host InAs NW periods a . Insets show bird's-eye view SEM images of vertical MnAs/InAs heterojunction NWs with a values of 0.5, 1.0, and 3.0 μm , in order from left to right. MnAs NCs were grown at 580 °C for 1 min by utilizing endotaxy. (b) The average height of NWs was estimated using 100 randomly chosen NWs observed in SEM images. They are plotted as a function of the number of MnAs NCs formed in the middle of NWs. Inset shows a bird's-eye view SEM image of vertical heterojunction NWs, which had MnAs NCs grown at 580 °C for 1 min. (c) The average size of MnAs NCs formed on top {111}B crystal facets of host InAs NWs, W_{top} , and the distance between MnAs NCs, D_c , were estimated

using 100 randomly chosen NWs. They are plotted as a function of growth temperatures T_g of NCs and are defined in the inset.36

Figure 4-6 Bird's-eye view SEM images of vertical MnAs/InAs hybrid and heterojunction NWs in which MnAs NCs were grown at (a) 580, (b) 540, (c) 490, and (d) 400 °C for 1 min. Insets in (a) to (c) are schematics in which MnAs NCs are indicated by dark gray dots in and on bright gray InAs NWs. It was highly possible that the host InAs NWs in (d) was already lower than the other NWs in (a) to (c) before the NC formation. It was difficult to estimate the vertical distance between the MnAs NCs, D_c , for the NCs grown at 400 °C for 1 min in the host InAs NWs because the NCs formed too closely to one another to identify. However, we observed a tendency consistent with that obtained in Figure 4-5(c).37

Figure 4-7 Bird's-eye view SEM images of vertical MnAs/InAs heterojunction NWs, in which MnAs NCs were grown at 580 °C for (a) 1, (b) 2, and (c) 5 min, respectively. (d) Schematic illustration for the definition of parameters used in Figures 4-7(e) and 4-7(f), H_{top} , H_{mid} , W_{top} , W_{mid} , L_{up} , L_{low} , D_{up} , and D_{low} . (e) Average height and width of MnAs NCs were estimated using 100 randomly chosen heterojunction NWs observed in SEM images. The average height and width of top NCs are defined as H_{top} and W_{top} , and those of middle NCs are H_{mid} and W_{mid} , respectively. They are plotted as a function of the growth time, t , of MnAs NCs. (f) Average length and diameter of InAs NWs were estimated using 100 randomly chosen heterojunction NWs observed in SEM images. The average length and diameter of an upper part of InAs NWs, NW_{up} , are defined as L_{up} and D_{up} , and those of a lower part of NWs, NW_{low} , are L_{low} and D_{low} , respectively. The D_{up} , D_{low} , and the percentage of L_{up} to the whole length of InAs NWs, i.e., $L_{up} + L_{low}$, are plotted as a function of the t of MnAs NCs. © 2017 The Japan Society of Applied Physics [R. Kodaira *et al.*, Jpn. J. Appl. Phys. **56**, 06GH03 (2017)].39

Figure 5-1 (a) A top view secondary electron image and (b) a corresponding MFM image of one of MnAs/InAs heterojunction NWs. The MFM image was observed in the conventional PD mode of the MFM system. (c)–(f) Highly magnified MFM images of NCs I and II, which were observed in the AD mode of the MFM system. (c, e) High and (d, f) low drive frequencies were set in the AD

-
- mode measurements. The reversals in contrasts of NCs I and II by changing the drive frequency clearly showed that magnetic responses were obtained from them.48
- Figure 5-2 (a) A top view BSE image of the MnAs/InAs heterojunction NWs. Inset of (a) is a highly magnified BSE image of NC III with a relatively large height and aspect ratio R , which is defined as $R = \text{NC's height}/\text{NC's width}$, of approximately 1.1. (b)-(e) Corresponding highly magnified MFM images of NC III at room temperature. External magnetic fields \mathbf{B} of 2 kG were applied in the directions indicated by the thick white arrows in the figures. MFM images of (c) and (e), in particular, were taken with a reversely-magnetized MFM tip, i.e., the magnetized direction of MFM tip opposite to that used in (b) and (d), respectively, to ensure that the obtained dark-bright contrast series observed in the NC III region was due to the magnetic responses from the NC III. Thin white arrows indicate the possible magnetization directions \mathbf{M} of the NC III.50
- Figure 5-3 (a) A top view BSE image of a bended MnAs/InAs heterojunction NW laid on a SiO₂/Si substrate. Regions with bright and dark contrasts in the NW were due to InAs and MnAs, respectively. The $\langle 111 \rangle_B$ directions of the host InAs NW were markedly tilted at the position where the MnAs NC V was formed. The inset shows a corresponding AFM image of MnAs NCs IV and V. White dotted lines in the inset represent cross-sectional planes of cross-sectional line profiles of (b) NC V, (c) NC IV, and (d) NCs IV and V (i.e., NC IV-V) observed by AFM.52
- Figure 5-4 (a)-(g) Top view MFM images of MnAs NCs IV and V observed at room temperature, in which white scale bars represent 100 nm. The external magnetic fields \mathbf{B} of 2 to 5.7 kG were applied before the MFM observations of (a), (c), (e), (f), and (g). MFM images of (b) and (d) were taken with a reversely magnetized MFM tip, i.e., the magnetized direction of the MFM tip opposite to that used in (a) and (c), respectively, to ensure that the obtained bright-dark contrast series observed in the NC IV and V regions were due to the magnetic responses from the NCs. All the gray circles marked by M_{IV} and M_V as an inset in (a)-(g) show “cross-sectional” schematic illustrations depicting the possible magnetizations, M_{IV} and M_V , which are drawn by black

arrows in the gray circles, of NCs IV and V, respectively. White dotted lines in (a) indicate the cross-sectional planes of the schematic illustrations. (h) Cross-sectional illustration showing a possible magnetic response from the NC V when the NC V was magnetized along the magnetization direction of the MFM tip.54

Figure 5-5 (a)-(d) Top view MFM images of NCs IV and V observed at temperature, in which white scale bars represent 100 nm. The external magnetic fields \mathbf{B} of 5.7 kG were applied perpendicular to the SiO₂/Si substrate surface before the MFM observations of (a) and (c). Just after the MFM observations of (a) and (c), MFM images of (b) and (d) were taken in series, respectively, with a reversely magnetized MFM tip, i.e., the magnetized direction of the MFM tip opposite to that used in (a) and (c), respectively. Therefore, the serial MFM observations were carried out in the order of (a)-(b) and (c)-(d), respectively, as shown by black-dotted arrows between the images. All the gray circles in (a)-(d) show “cross-sectional” schematic illustrations depicting the possible magnetizations, M_{IV} and M_V , which are drawn by black arrows in the gray circles, of NCs IV and V, respectively. White dotted lines in (a) indicate the cross-sectional planes of the schematic illustrations.55

Figure 6-1 Temperature dependence of the resistance R of the single NW samples (a) NW15C and (b) NW34B. The insets in (a) and (b) show top view SEM images of NW15C and NW34B, respectively. The activation energies E_A are roughly estimated in the temperature range from 200 to 280 K. A larger R and E_A of NW34B compared to that of NW15C possibly arises from a larger contact resistance in the two-terminal measurements, caused by different surface treatments used to etch off the native oxide at the contact areas.64

Figure 6-2 (a) Temperature dependence of the magnetoresistance (MR) of NW15C. The MR is defined as $MR = [R(\mathbf{B}, T) - R(0, T)]/[R(0, T)]$, where $R(\mathbf{B}, T)$ is the resistance R at an external magnetic field \mathbf{B} and at a temperature T . \mathbf{B} was applied from 0 to 10 T perpendicular to the InAs NW axis as represented by the white thick arrow in the inset of (a). (b) Magnification of (a) in the magnetic field range from 0 to 3 T. Universal conductance fluctuations and a negative MR due to weak localization are observed at lower T65

Figure 6-3 (a) Angle dependence of the magnetoresistance (MR) of NW34B at 120 K for different external magnetic fields \mathbf{B} . The angle-dependent MR is defined as $MR = [R(\theta) - R(0)]/[R(0)]$, where $R(\theta)$ is the resistance R at an angle θ between \mathbf{B} and the NW axis as schematically illustrated in the inset. The maximum MR at $\mathbf{B} = 10$ T is observed at θ_{crit} of approximately 60° . (b)-(d) Schematic illustrations of the electron trajectories, indicated by black arrows, with an additional diffusive boundary scattering contribution in the channel width W . The radius of the cyclotron orbits r_{cycl} decreases with increasing θ . (c) When $r_{\text{cycl}} \approx 2W$, the maximum backscattering led to a maximum in R and the MR [C. W. J. Beenakker *et al.*, *Solid State Physics* **44**, 1 (1991)].66

Figure 6-4 (a) A top view SEM image of NW01B, which has at least two MnAs NCs between the electrical contacts as marked by white circles. (b) Temperature dependence of the magnetoresistance (MR) of NW01B. The MR is defined as $MR = [R(\mathbf{B}, T) - R(0, T)]/[R(0, T)]$, where $R(\mathbf{B}, T)$ is the resistance R at an external magnetic field \mathbf{B} and at a temperature T . \mathbf{B} was applied from 0 to 10 T perpendicular to the NW axis as represented by the white thick arrow in (a). The linear negative MR at low T indicated the formation of magnetic polarons [S. Kumar *et al.*, *Nano Lett.* **13**, 5079 (2013), A. Kaminski *et al.*, *Phys. Rev. Lett.* **88**, 248212 (2002)] by Mn-atoms in the host NW, due to non-intentional doping and/or thermal diffusion of Mn atoms from MnAs NCs during the endotaxial growth of MnAs NCs.68

List of Tables

Table 4-1	The standard enthalpies for the formation reactions of the elements ΔH_f (kJ mol ⁻¹) for MnP, GaP, MnAs, InAs, and GaAs at 700, 800, and 900 (K) [I. Barin, <i>Thermochemical Data of Pure Substances</i> (Wiley-VCH, Weinheim, 1989)].33
Table 6-1	Properties of the different single NW samples investigated in this study. The NW length L between electrical contacts and the NW diameter d are roughly estimated from top view SEM images. The resistance R at 280 K and the activation energies E_A are taken from the results of the temperature dependent measurements.63

Chapter 1

Introduction

1.1 Background

1.1.1 Vertical semiconducting nanowires

Miniaturization of electronic components in accordance with Moore's law [1] has brought about today's great progress in electronics industry. However, the miniaturization processes of semiconductor electronics and magnetoelectronics devices are approaching their technological limits. To realize the improvement of the electronics device performance beyond the conventional Si-based technology, new ideas, such as devices using new design, new materials, new fabrication/assembly methods, and new functionalities, have to be developed, and they are intensely studied in recent years [2-6]. Among them, vertical free-standing semiconducting nanowires (NWs) have attracted much attention as one of the promising candidates for not only next-generation electronic but also photonic, sensing, and spintronic devices [7-20]. In addition, semiconducting NWs are recently of great interest owing to their great emission efficiency in the terahertz spectral range [21-23]. Vertical semiconducting NWs are geometrically suitable for creating a vertical surrounding gate (VSG) structure in vertical field-effect transistors (FETs) [24, 25], which possess advantageous device characteristics such as high current on-off ratio and reduced short channel effects owing to the high gate controllability of the VSG structure. For example, practical ways of installing VSG-FETs using NWs for current integrated circuits based on CMOS technologies have been demonstrated [26]. Most of these NWs reported elsewhere have thus far been synthesized and demonstrated by using some of the most popular bottom-up fabrication techniques in the world, i.e., vapor-liquid-solid (VLS) methods that typically use gold nanoparticles as catalysts. However, conventional metal catalysts used in the VLS method possibly lead to the deterioration of performance of NW devices mainly due to deep level formation by incorporated metal impurities. In addition, the VLS-grown NWs are randomly distributed on a semiconducting substrate in most cases, which might hinder the practical

applications of NWs in devices in the future. We, on the other hand, have demonstrated the catalyst-free formation of vertical free-standing semiconducting NW arrays, e.g., GaAs, InGaAs, InP, InAs, GaAs/AlGaAs core-shell, and GaAs/GaAsP core-shell NWs, by selective-area metal-organic vapor phase epitaxy (SA-MOVPE) using partially SiO₂-masked {111}A and B substrates, which has enabled us to control the size, aspect ratio, position, and density of NWs on various semiconducting substrate materials [27, 28]. Nanoelectronic devices such as VSG-FETs have been fabricated, and their performance has been demonstrated using our semiconducting NWs grown by SA-MOVPE for future device applications [29, 30].

1.1.2 Hybrid structures between magnetic and semiconducting materials

In the nanospintronic research fields, the heteroepitaxy of ferromagnetic and III-V compound semiconductors (FM III-V hybrids) have attracted a great deal of attention due to possible additional functionalities that have been added to current semiconducting devices and integrated circuits. Among them, granular hybrid structures containing ferromagnetic nanoclusters (NCs) embedded into semiconductor layers are one of the most attractive candidates for future nanospintronic devices because it has been reported that they have huge magnetoresistance (MR) effects, a relatively long spin-relaxation time, and interesting magnetotransport properties [6, 31-33]. Various kinds of NWs with FM III-V hybrids have been synthesized to produce NW spintronic devices by using several techniques based on conventional VLS methods as bottom-up fabrication approaches, e.g., MnAs nanoparticles on InAs [34] and GaAs [20, 35] NWs and GaAs/MnAs core-shell NWs [36, 37]. However, it is also crucial to avoid and overcome the possible problems caused in the current nanoelectronic and photonic NW devices created with these conventional VLS methods particularly in the future on the way towards practical NW spintronic devices. Therefore, we have developed hybridization techniques of ferromagnetic MnAs NCs [38] on vertical free-standing semiconducting NW templates grown by using our catalyst-free SA-MOVPE technique [27, 28] in the research fields of semiconductor nanospintronics, and reported on the formation and characterizations of MnAs NC/GaAs hybrid NWs [39, 40]. We developed an SA-MOVPE technique in our previous studies to directly

synthesize single-crystal ferromagnetic MnAs NCs on a semiconducting substrate, and we demonstrated that the NCs could be used as promising building blocks for fabricating nanospintronic devices of the future since they demonstrated large angle-dependent MR effects. However, we realized that it is still difficult to form vertical heterojunction NWs between ferromagnetic MnAs and semiconducting layers, which would enable us to inject spin-polarized carriers and currents into semiconducting NW channels. It is also difficult to control the crystal orientations of MnAs NCs in a $\langle 111 \rangle$ B-oriented GaAs NW template [39, 40] and to obtain atomically abrupt heterointerfaces between MnAs and GaAs even when using our hybridization techniques. It is likely that the difficulty in forming vertical heterojunction NWs was mainly due to the relatively stable crystal facet of the c-plane, i.e., the $\{0001\}$ -oriented surface, at the surface of hexagonal NiAs-type MnAs NCs grown by SA-MOVPE [39]. Thus, we investigated the formation of MnAs NCs on different III-V compound semiconducting NW templates, such as GaAs/AlGaAs core-shell, GaAs/GaAsP core-shell, and InAs NW templates [41]. For the InAs NW templates, MnAs NCs were grown much deeper into the InAs NWs compared to the other NWs and their crystal axes could be well-controlled in the InAs NWs. These results indicate that the possibility of formation of vertical MnAs/InAs heterojunction NWs and the controllability of magnetizations of MnAs NCs in the vertical heterojunction NWs, which are advantage to create NW-based nanospintronic devices. Some of the further main reasons why we have focused on the vertical MnAs/InAs heterojunction NWs are listed as follows. (i) In the case of the vertical free-standing NWs, we can expect nanometer-scale heterojunctions with misfit-dislocation-free heterointerfaces of with a drastically-decreased number of misfit dislocations compared to flat layers, even in the case of materials system with a lattice mismatch larger than 10% [42]. (ii) A c-plane of hexagonal NiAs-type MnAs has a similar atomic arrangement to a $\{111\}$ B plane of zinc-blende-type InAs. In addition, theoretical calculations indicate that zinc-blende-type MnAs is half-metallic [43], and we can expect the growth of zinc-blende-type MnAs in the heterojunction NWs by crystal structure transfer in vertical free-standing NWs [44]. (iii) These two materials, MnAs and InAs, both have arsenic atoms as group V element, which leads to avoiding a possible intermixing problem at heterointerfaces. (iv) Hexagonal α -phase MnAs shows a ferromagnetism above room temperature. Ferromagnetic metals with much higher Curie temperature, T_c , e.g., hexagonal NiAs-type MnSb with T_c of 588 K [45], might be also promising as well as half-metallic zinc-blende-type MnAs. If the vertical heterojunction NWs with atomically-abrupt

heterointerfaces between ferromagnetic MnAs NCs and semiconducting InAs NWs are formed, it would enable us to inject spin-polarized carriers and currents into semiconducting NW channels. InAs is well-known as a promising candidate channel material for nanospintronic devices, e.g., for Datta-Das-type spin-FETs [46], because of its high electron mobility and strong spin-orbit interaction [47]. In addition, $\langle 111 \rangle$ B-oriented semiconducting InAs NW channels possibly have a great advantage to enhance spin-lifetime in the channels of nanospintronic devices [48]. Thus, we believe that the combination of a magnetic tunnel junction electrodes with the vertical MnAs/InAs heterojunction NWs with atomically-abrupt heterointerfaces [49] could overcome major obstacles, namely, conductance mismatch and poor controllability in the formation of heterointerfaces in current nanospintronic devices. Furthermore, an efficient gate controllability of a solid electrolyte surrounding gate with InAs NW channels was reported [50]. Therefore, the vertical MnAs/InAs heterojunction NWs with our VSG-FET structures [29, 30] may provide new possibilities and versatility in the creation of novel magneto-nanoelectronic or nanospintronic devices using vertical free-standing semiconducting NWs.

1.2 Objective

As described in the previous section, the vertical MnAs/InAs heterojunction NWs have tremendous potential for applications in next-generation nanoelectronic or nanospintronic devices. Therefore, the main objective of this study is synthesis of the vertical ferromagnetic MnAs/semiconducting InAs heterojunction NWs with atomically-abrupt heterointerfaces. To create devices using the MnAs/InAs heterojunction NWs with our VSG-FET structures, it is crucial to control the size, shape, magnetization of MnAs NCs in the heterojunction NWs and to understand their structural, magnetic, transport properties. Thus, we first report on the synthesis of the vertical MnAs/InAs heterojunction NWs and their possible growth mechanism on the basis of detailed structural characterization and growth condition dependences. Additionally, magnetizations and magnetotransport characterizations are performed towards application of the heterojunction NWs to novel magneto-nanoelectronic or nanospintronic devices with our VSG-FET structures.

1.3 Outline of this thesis

This thesis describes the synthesis and characterizations of the vertical ferromagnetic MnAs/semiconducting InAs heterojunction NWs aimed at the creation of the novel magneto-nanoelectronic or nanospintronic devices using vertical semiconducting NWs. This thesis is divided into 7 chapters.

In chapter 2, the history and advantages of nanowires are described. In addition, the methods of the catalyst-assisted VLS growth and the SA-MOVPE growth are explained.

In chapter 3, the principle and system of MOVPE, which is utilized in order to grow the vertical ferromagnetic MnAs/semiconducting InAs heterojunction NWs in this study, are explained. In addition, the fabrication techniques of the vertical heterojunction NWs and the lateral NW samples for magnetization and magnetotransport characterizations are described. Finally, the characterization methods and equipment used in this study are also introduced.

In chapter 4, growth of vertical ferromagnetic MnAs/semiconducting InAs heterojunction NWs on GaAs (111)B substrates by combining the catalyst-free SA-MOVPE of InAs NWs and the endotaxial nanoclustering of MnAs is described. The desorption of As and/or In atoms in the host InAs NWs, The NW length, and the surface migration length of Mn adatoms on the NWs are the keys to the successful fabrication of vertical MnAs/InAs heterojunction NWs with atomically-abrupt heterointerfaces. A possible growth mechanism of MnAs NCs is discussed on the basis of detailed structural characterization and growth condition dependence results.

In chapter 5, magnetizations and magnetic domains of ferromagnetic MnAs NCs in MnAs/InAs heterojunction NWs investigated by magnetic force microscopy are described. MnAs NCs magnetized along a-axes, i.e., magnetic easy axis of hexagonal NiAs-type MnAs, are generally observed, which are consistent with the structural characterization results in chapter 4. For some MnAs NCs, we occasionally observed the magnetization along the c-axes due to a shape anisotropy and the small coercivity of NCs formed at a markedly bending position in the bended MnAs/InAs heterojunction NWs.

In chapter 6, magnetotransport properties of single undoped-InAs and MnAs/InAs heterojunction NWs are described. The single InAs NWs show universal conductance fluctuations, a negative magnetoresistance at low temperature as well as an ordinary positive magnetoresistance. In contrast, the MnAs/InAs heterojunction NWs show a linear negative magnetoresistance possibly due to the formation of magnetic polarons.

Bibliography

- [1] G. E. Moore, *Electronics* **38**, 114 (1965).
- [2] M. T. Bohr and I. A. Young, *IEEE Micro* **37**, 20 (2017).
- [3] S. Manipatruni, D. E. Nikonov, and I. A. Young, *Nat. Physics* **14**, 338 (2018).
- [4] A. D. Franklin, *Science* **349**, aab2750 (2015).
- [5] S. Sugahara and J. Nitta, *Proc. IEEE* **98**, 2124 (2010).
- [6] M. T. Elm and S. Hara, *Adv. Mater.* **26**, 8079 (2014).
- [7] X. Duan, Y. Huang, Y. Cui, J. Wang, and C. M. Lieber, *Nature* **409**, 66 (2001).
- [8] J. Wang, M. S. Gudiksen, X. Duan, Y. Cui, and C. M. Lieber, *Science* **293**, 1455 (2001).
- [9] Y. Cui and C. M. Lieber, *Science* **291**, 851 (2001).
- [10] C. Thelander, T. Matensson, M. T. Björk, B. J. Ohlsson, M. W. Larsson, L. R. Wallenberg, and L. Samuelson, *Appl. Phys. Lett.* **83**, 2052 (2003).
- [11] X. Duan, Y. Huang, R. Agarwal, and C. M. Lieber, *Nature* **421**, 241 (2003).
- [12] D. Zhang, C. Li, X. Liu, S. Han, T. Tang, and C. Zhou, *Appl. Phys. Lett.* **83**, 1845 (2003).
- [13] P. Offermans, M. Crego-Calama, and S. H. Brongersma, *Nano Lett.* **10**, 2412 (2010).
- [14] B. Tian, X. Zheng, T. J. Kempa, Y. Fang, N. Yu, G. Yu, J. Huang, and C. M. Lieber, *Nature* **449**, 885 (2007).
- [15] J. Wallentin, N. Anttu, D. Asoli, M. Huffman, I. Åberg, M. H. Magnusson, G. Siefert, P. Fuss-Kailuweit, F. Dimroth, B. Witzigmann, H. Q. Xu, L. Samuelson, K. Deppert, and M. T. Borgström, *Science* **339**, 1057 (2013).
- [16] N. Han, F. Wang, J. J. Hou, S. P. Yip, H. Lin, F. Xiu, M. Fang, Z. Yang, X. Shi, G. Dong, T. F. Hung, and J. C. Ho, *Adv. Mater.* **25**, 4445 (2013).
- [17] Y. J. Hong, J. W. Yang, W. H. Lee, R. S. Ruoff, K. S. Kim, and T. Fukui, *Adv. Mater.* **25**, 6847 (2013).
- [18] P. Ren, W. Hu, Q. Zhang, X. Zhu, X. Zhuang, L. Ma, X. Fan, H. Zhou, L. Liao, X. Duan, and A. Pan, *Adv. Mater.* **26**, 7444 (2014).
- [19] N. P. Dasgupta, J. Sun, C. Liu, S. Brittman, S. C. Andrews, J. Lim, H. Gao, R. Yan, P. Yang, *Adv. Mater.* **26**, 2137 (2014).
- [20] J. Hubmann, B. Bauer, H. S. Körner, S. Furthmeier, M. Buchner, G. Bayreuther, F. Dirnberger, D. Schuh, C. H. Back, J. Zweck, E. Reiger, D. Bougeard, *Nano Lett.* **16**, 900 (2016).
- [21] D. V. Seletskiy, M. P. Hasselbeck, J. G. Cederberg, A. Katzenmeyer, M. E. Toimil-Molares,

- F. Léonard, A. A. Talin, and M. Sheik-Bahae, *Phys. Rev. B* **84**, 115421 (2011).
- [22] V. N. Trukhin, A. S. Buyskikh, N. A. Kaliteevskaya, A. D. Bouravleuv, L. L. Samoilov, Yu. B. Samsonenko, G. E. Cirilin, M. A. Kaliteevski, and A. J. Gallant, *Appl. Phys. Lett.* **103**, 072108 (2013).
- [23] A. Arlauskas, J. Treu, K. Saller, I. Beleckaite, G. Koblmüller, A. Krotkus, *Nano Lett.* **14**, 1508 (2014).
- [24] H. T. Ng, J. Han, T. Yamada, P. Nguyen, Y. Chen, and M. Meyyappan, *Nano Lett.* **4**, 1247 (2004).
- [25] V. Schmidt, H. Riel, S. Senz, S. Karg, W. Riess, and U. Gösele, *Small* **2**, 85 (2006).
- [26] T. H. Bao, D. Yakimets, J. Ryckaert, I. Ciofi, R. Baert, A. Veloso, J. Boemmels, N. Collaert, P. Roussel, S. Demuyne, P. Raghavan, A. Mercha, Z. Tokei, D. Verkest, A. V-Y. Thean, and P. Wambacq, *Proc. the 44th European Solid-State Device Research Conference (ESSDERC 2014)*, 102 (2014).
- [27] T. Sato, Y. Kobayashi, J. Motohisa, S. Hara, and T. Fukui, *J. Cryst. Growth* **310**, 5111 (2008).
- [28] K. Tomioka, J. Motohisa, S. Hara, and T. Fukui, *Nano Lett.* **8**, 3475 (2008).
- [29] T. Tanaka, K. Tomioka, S. Hara, J. Motohisa, E. Sano, and T. Fukui, *Appl. Phys. Express* **3**, 025003 (2010).
- [30] Y. Kobayashi, Y. Kohashi, S. Hara, and J. Motohisa, *Appl. Phys. Express* **6**, 045001 (2013).
- [31] P. N. Hai, S. Ohya, M. Tanaka, S. E. Barnes, and S. Maekawa, *Nature* **458**, 489 (2009).
- [32] P. N. Hai, S. Ohya, and M. Tanaka, *Nat. Nanotechnol.* **5**, 593 (2010).
- [33] M. Tanaka, S. Ohya, and P. N. Hai, *Appl. Phys. Rev.* **1**, 011102 (2014).
- [34] D. G. Ramlan, S. J. May, J. G. Zheng, J. E. Allen, B. W. Wessels, and L. J. Lauhon, *Nano Lett.* **6**, 50 (2006).
- [35] M. F. H. Wolff, D. Görlitz, K. Nielsch, M. E. Messing, and K. Deppert, *Nanotechnology* **22**, 055602 (2011).
- [36] M. Hilse, Y. Takagaki, J. Herfort, M. Ramsteiner, C. Herrmann, S. Breuer, L. Geelhaar, and H. Riechert, *Appl. Phys. Lett.* **95**, 133126 (2009).
- [37] J. Liang, J. Wang, A. Paul, B. J. Cooley, D. W. Rench, N. S. Dellas, S. E. Mohny, R. Engel-Herbert, and N. Samarth, *Appl. Phys. Lett.* **100**, 182402 (2012).
- [38] S. Hara, D. Kawamura, H. Iguchi, J. Motohisa, and T. Fukui, *J. Cryst. Growth* **310**, 2390 (2008).

-
- [39] M. Yatago, H. Iguchi, S. Sakita, and S. Hara, *Jpn. J. Appl. Phys.* **51**, 02BH01 (2012).
- [40] S. Hara, S. Sakita, and M. Yatago, *Jpn. J. Appl. Phys.* **51**, 11PE01 (2012).
- [41] S. Hara, H. Fujimagari, S. Sakita, and M. Yatago, *Proc. SPIE* **8820**, 88200V (2013).
- [42] K. Tomioka, M. Yoshimura, and T. Fukui, *Nano Lett.* **13**, 5822 (2013).
- [43] M. Shirai, T. Ogawa, I. Kitagawa, and N. Suzuki, *J. Magn. Magn. Mater.* **177-181**, 1383 (1998).
- [44] F. Ishizaka, Y. Hiraya, K. Tomioka, and T. Fukui, *J. Cryst. Growth* **411**, 71 (2015).
- [45] V. S. Bai and K. V. S. R. Rao, *J. Appl. Phys.* **55**, 2167 (1984).
- [46] S. Datta and B. Das, *Appl. Phys. Lett.* **56**, 665 (1990).
- [47] T. Matsuda and K. Yoh, *Physica E* **42**, 979 (2010).
- [48] K. Biermann, A. Hernandez-Minguez, R. Hey, and P. V. Santos, *J. Appl. Phys.* **112**, 083913 (2012).
- [49] J. Tang, C.-Y. Wang, M.-H. Hung, X. Jiang, L.-T. Chang, L. He, P.-H. Liu, H.-J. Yang, H.-Y. Tuan, L.-J. Chen, and K.-L. Wang, *ACS Nano* **6**, 5710 (2012).
- [50] D. Liang and X. P. A. Gao, *Nano Lett.* **12**, 3263 (2012).

Chapter 2

Semiconducting Nanowires

Semiconducting nanowires have attracted much attention since the 1960s because of their tremendous potential for applications in next-generation electronic, photonic, biochemical sensing, and even spintronic devices. This chapter describes the research history, advantages, and growth methods of semiconducting nanowires.

2.1 Introduction

2.1.1 History of nanowire growth

Study on nanowires (NWs) growth and their device applications have recently become more active in the nanoscience research fields. The number of reports on NWs has been increasing as shown in Figure 2-1. The NWs originated from the vapor-liquid-solid (VLS) growth of Si whisker using gold as a catalyst reported by Wagner and Ellis at Bell Laboratory in 1964 [1]. The “nanowire” was initially called as “whisker”, and then it changed to “nano-pillar”, “nano-rod”, “nano-column”, or “nano-wire”. In the early 1990s, the first device application with p-n junction in GaAs whiskers grown by VLS method was reported by Hiruma’s group at Central Research Laboratory, Hitachi Ltd [2, 3]. After that, various type of NWs grown by VLS method and their applications were demonstrated in the world. For example, the Lieber’s group at Harvard University in USA [4-6], the Yang’s group at University of California, Berkley in USA [7], and the Samuelson’s group at Lund University in Sweden [8, 9]. On the other hand, the Fukui’s group at Hokkaido University in Japan has reported on the catalyst-free selective-area metal-organic vapor phase epitaxy (SA-MOVPE) of III-V compound semiconducting NWs, such as InGaAs [10], InP [11], GaAs [12], and InAs [13] NWs.

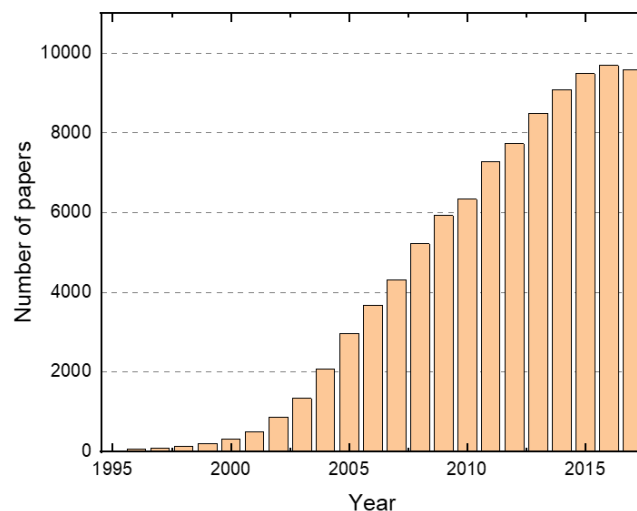


Figure 2-1. Number of published papers about NW is plotted as a function of year. Data was obtained from the Web-of-Science database with the following combination of keywords, “topic = nanowire or nanowires”.

2.1.2 Advantages of nanowire

The NWs are wire-like nanostructures with small diameters below about one hundred and several tens nanometers and with high aspect ratios, which enable novel electrical properties different from the conventional bulk structures. The vertical semiconducting NWs are expected to possess potentiality of high-density integration due to their small footprint. In addition, their small diameters allow heteroepitaxial growth with lattice mismatch material systems in the axial direction of NW growth. Grass reported on the relation between the critical diameters of NWs and the lattice mismatch [14]. This gives a wider selection of heteroepitaxial material combinations, such as III-V compound semiconducting NW on Si or Ge substrates [15, 16], and new opportunity of heteroepitaxial growth of magnetic and semiconducting materials. If the high quality heterointerfaces between magnetic and semiconducting layers are formed, major obstacles of conductance mismatch and poor controllability in the formation of heterointerfaces in current nanospintronic devices could be overcome. Another advantage of vertical NWs is their structures

which are geometrically suitable for creating a vertical surrounding gate (VSG) structure in vertical field-effect transistors (FETs) [17-20], which possess advantageous device characteristics such as high current on-off ratio and reduced short channel effects owing to the high gate controllability of the VSG structure. For instance, an efficient gate controllability of a solid electrolyte surrounding gate to tune spin-orbit interaction in single InAs NW channels was reported [21].

2.2 Nanowire growth methods

2.2.1 Catalyst-assisted vapor-liquid-solid growth

Figure 2-2 shows a schematic illustration of the procedure of the catalyst-assisted VLS growth of a vertical free-standing Si NW on a Si substrate. At first, Au seed particle is deposited on the Si substrate. Increasing temperature and supplying Si source materials lead to the incorporation of Si atoms into Au droplet, and then Au-Si liquid alloy is formed. The incorporation continues until the Au-Si alloy becomes supersaturated. Consequently, crystal growth occurs at the solid-liquid interfaces and NW growth starts with a diameter depending on the size of the Au droplet. The droplet generally remains at the top of the NW after the NW growth. It leads to the deterioration of performance of NW devices mainly due to deep level formation by incorporated

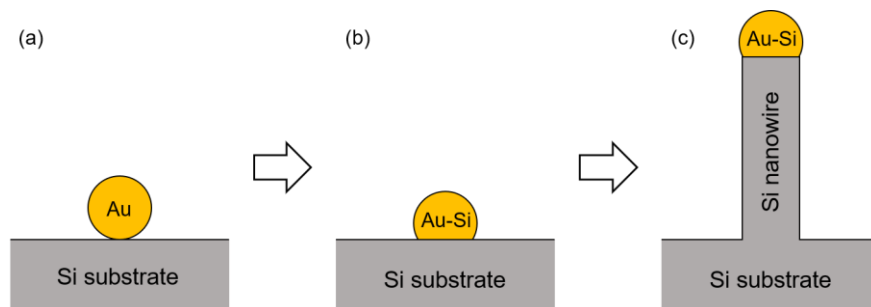


Figure 2-2. Schematic illustration of VLS growth of a Si NW using a Au catalyst. (a) The Au seed particle is deposited on the substrate. (b) Au-Si liquid alloy is formed by heating and supplying Si source materials. (c) Nucleation occurs at the interface between the liquid alloy and the substrate surface, and then NW begins to grow.

metal impurities [22]. To solve this issue, alternative method was introduced, where NWs are grown without Au or other metal catalysts. It is known as “self-catalyzed growth”. In this method, one component of the nanowire materials is used as a catalytic droplet, which enables NW growth in the VLS mechanism without the metal impurities. For instance, NWs grown by the self-catalyzed growth method were reported [23-25]. In addition, another problem of the VLS growth is that NWs are randomly distributed on a semiconducting substrate in most cases, which might hinder the practical applications of NWs in devices in the future. To control of the NW position, the metal seed particles positioned by lithography process were introduced [26].

2.2.2 Selective-area metal-organic vapor phase epitaxy

SA-MOVPE is a catalyst-free method using partially SiO_2 -masked semiconducting substrates, which has enabled us to control the size, aspect ratio, position, and density of NWs on various semiconducting substrate materials [15, 27]. Therefore, SA-MOVPE method can overcome major obstacles of VLS method, namely, the impurities from the metal seed catalyst and the randomness of NW position. Figure 2-3 shows a schematic illustration of NW growth process of the catalyst-free SA-MOVPE method. First, SiO_2 thin films are deposited on the semiconducting substrates. Initial circular openings in the SiO_2 thin films are next fabricated by lithography and etching techniques. Finally, nucleation occurs on the substrate surface within the mask opening regions, and then the NW begins to grow by supplying organometallic and hydride sources.

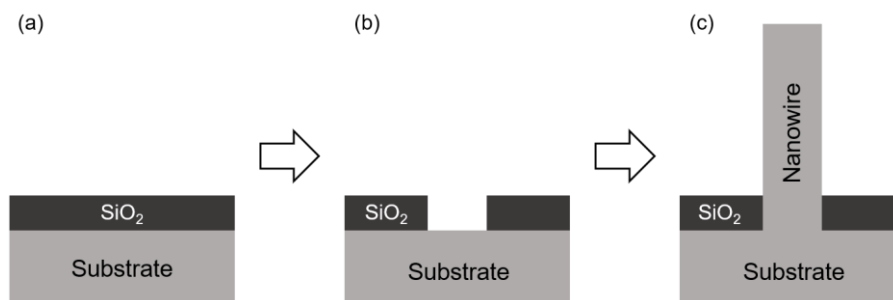


Figure 2-3. Schematic illustration of catalyst-free SA-MOVPE growth. (a) SiO_2 thin film is deposited on the substrate. (b) Initial circular openings are fabricated in the SiO_2 thin film by lithography and etching. (c) Nucleation occurs on the substrate surface within the mask opening region, and then NW begins to grow.

Bibliography

- [1] R. S. Wagner and W. C. Ellis, *Appl. Phys. Lett.* **4**, 89 (1964).
- [2] K. Hiruma, T. Katsuyama, K. Ogawa, M. Koguchi, H. Kakibayashi, and G. Morgan, *Appl. Phys. Lett.* **59**, 431 (1991).
- [3] K. Haraguchi, T. Katsuyama, K. Hiruma, and K. Ogawa, *Appl. Phys. Lett.* **60**, 745 (1992).
- [4] X. Duan, J. Wang, and C. M. Lieber, *Appl. Phys. Lett.* **76**, 1116 (2000).
- [5] Y. Cui, Q. Wei, H. Park, and C. M. Lieber, *Science* **293**, 1289 (2001).
- [6] X. Duan, Y. Huang, Y. Cui, J. Wang, and C. M. Lieber, *Nature* **409**, 66 (2001).
- [7] M. H. Huang, S. Mao, H. Feick, H. Yan, Y. Wu, H. Kind, E. Weber, R. Russo, and P. Yang, *Science* **292**, 1897 (2001).
- [8] B. J. Ohlsson, M. T. Björk, M. H. Magnusson, K. Deppert, L. Samuelson, and L. R. Wallenberg, *Appl. Phys. Lett.* **79**, 3335 (2001).
- [9] C. Thelander, T. Martensson, M. T. Bjork, B. J. Ohlsson, M. W. Larsson, L. R. Wallenberg, and L. Samuelson, *Appl. Phys. Lett.* **83**, 2052 (2003).
- [10] M. Akabori, J. Takeda, J. Motohisa, and T. Fukui, *Nanotechnology* **14**, 1071 (2003).
- [11] M. Inari, J. Takeda, J. Motohisa, and T. Fukui, *Phys. E Low-Dimensional Syst. Nanostructures* **21**, 620 (2004).
- [12] J. Noborisaka, J. Motohisa, and T. Fukui, *Appl. Phys. Lett.* **86**, 213102 (2005).
- [13] K. Tomioka, J. Motohisa, S. Hara, and T. Fukui, *Nano Lett.* **8**, 3475 (2008).
- [14] F. Glas, *Phys. Rev. B* **74**, 121302 (2006).
- [15] K. Tomioka, J. Motohisa, S. Hara, and T. Fukui, *Nano Lett.* **8**, 3475 (2008).
- [16] K. Tomioka, Y. Kobayashi, J. Motohisa, S. Hara, and T. Fukui, *Nanotechnology* **20**, 145302 (2009).
- [17] H. T. Ng, J. Han, T. Yamada, P. Nguyen, Y. Chen, and M. Meyyappan, *Nano Lett.* **4**, 1247 (2004).
- [18] V. Schmidt, H. Riel, S. Senz, S. Karg, W. Riess, and U. Gösele, *Small* **2**, 85 (2006).
- [19] T. Tanaka, K. Tomioka, S. Hara, J. Motohisa, E. Sano, and T. Fukui, *Appl. Phys. Express* **3**, 025003 (2010).
- [20] Y. Kobayashi, Y. Kohashi, S. Hara, and J. Motohisa, *Appl. Phys. Express* **6**, 045001 (2013).
- [21] D. Liang and X. P. A. Gao, *Nano Lett.* **12**, 3263 (2012).
- [22] J. E. Allen, E. R. Hemesath, D. E. Perea, J. L. Lensch-Falk, Z. Y. Li, F. Yin, M. H. Gass, P.

- Wang, A. L. Bleloch, R. E. Palmer, and L. J. Lauhon, *Nat. Nanotechnol.* **3**, 168 (2008).
- [23] A. F. i Morral, D. Spirkoska, J. Arbiol, M. Heigoldt, J. R. Morante, and G. Abstreiter, *Small* **4**, 899 (2008).
- [24] G. Zhang, S. Sasaki, K. Tateno, H. Gotoh, and T. Sogawa, *ALP Adv.* **3**, 052107 (2013).
- [25] B.-S. Kim, T.-W. Koo, J.-H. Lee, D. S. Kim, Y. C. Jung, S. W. Hwang, B. L. Choi, E. K. Lee, J. M. Kim, and D. Whang, *Nano Lett.* **9**, 864 (2009).
- [26] T. Sato, K. Hiruma, M. Shirai, K. Tominaga, K. Haraguchi, T. Katsuyama, and T. Shimada, *Appl. Phys. Lett.* **66**, 159 (1995).
- [27] T. Sato, Y. Kobayashi, J. Motohisa, S. Hara, and T. Fukui, *J. Cryst. Growth* **310**, 5111 (2008).

Chapter 3

Experimental Techniques

3.1 Introduction

This chapter describes nanowires (NWs) growth procedures, fabrication process of lateral NW samples, and characterization methods used in this study. The undoped host InAs NW templates are grown by selective-area metal-organic vapor phase epitaxy (SA-MOVPE), which is a catalyst-free and bottom-up NW fabrication method. The principles of MOVPE and the NW growth procedure by SA-MOVPE are described, and then the characterization methods are explained (refer to the previous study [1, 2]). In addition, fabrication process of lateral NW samples for magnetization and magnetotransport characterizations is also described.

3.2 Principles of MOVPE

3.2.1 Overviews

MOVPE is one of the bottom-up growth techniques using organometallic and hydride sources. Epitaxial growth is defined as a precise oriented growth of a single crystal material upon a surface of a single crystal substrate. Growing a layer with the same material as the substrate materials is called homoepitaxy and growing with different ones is therefore called heteroepitaxy. The epitaxial growth can be done by other representative methods, such as liquid phase epitaxy (LPE), vapor phase epitaxy (VPE), hydride vapor phase epitaxy (HVPE), and molecular beam epitaxy (MBE). MOVPE is often referred to as metal-organic chemical vapor deposition (MOCVD). But, we will use the term of MOVPE in this thesis to focus on particularly “epitaxy”.

3.2.2 MOVPE growth process

The key processes during the MOVPE growth have been summarized as listed below [3].

- i. Mass transport: The source materials are carried to the reactor by the carrier gas, and a boundary layer is formed above the substrate by the laminar flow of the vapor in the reactor. The molecules diffuse through the boundary layer toward the substrate surface.
- ii. Physical processes: During the molecules diffusion, molecules are adsorbed on appropriate lattice positions at kinks, steps, or are desorbed into the vapor phase. Two- or three-dimensional nucleation can take place at the substrate surface.
- iii. Chemical reactions: Surface reconstruction, adsorption/desorption processes of precursors, and density of steps/kinks/other defects strongly depend on the chemical reactions. Thermal decomposition of precursors under certain growth conditions should be considered.
- iv. Thermodynamics: the driving force for overall growth dominates the growth rate because it defines the deviation from equilibrium. Thus, it also affects the incorporation of native defects or dopants and surface stoichiometry.

Figure 3-1 shows schematic illustration of the mechanisms in the SA-MOVPE process. The growth rate is affected by the diffusion of growth species from the SiO₂ mask region and desorption to the outside of the boundary layer. To selectively grow NWs, the longer diffusion length of growth precursors is needed because the growth species dominantly diffuse from mask region to the opening area of the substrate surface. In order to avoid the depositions of poly-crystals on the mask surfaces, the high growth temperature and low working pressure are also needed because the poly-crystals prefer to deposit under the conditions where the high probability of encountering group-III species caused by the long resident time of the precursors on the surface.

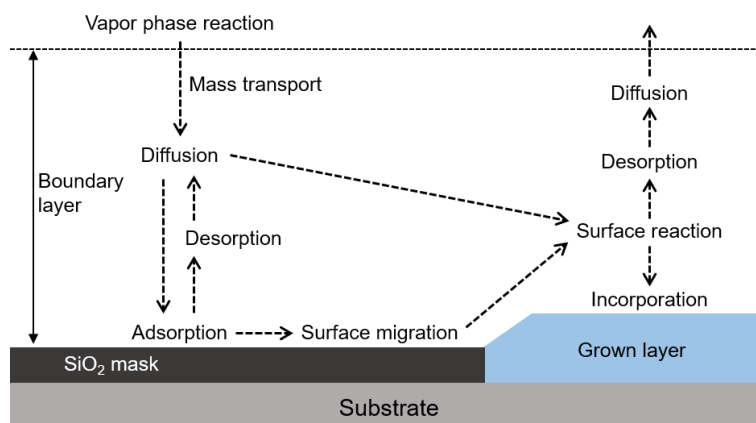


Figure 3-1. Schematic illustration of growth mechanism of SA-MOVPE process.

3.2.3 MOVPE growth system

Figure 3-2 shows schematic illustration of the MOVPE system utilized in this study. The MOVPE system consists of the gas delivery system, the horizontal reactor system with a temperature controller, and the low pressure pumping system. Palladium diffused purified hydrogen (H₂) is used as a carrier gas, which transports the source materials to the horizontal reactor. The gas and MO sources are provided from gas cylinders and bubblers, respectively. Figure 3-3 shows schematic illustration of the bubblers, which are kept at a constant temperature to control the amount of material supply. The partial pressure of MO sources is controlled by mass-flow controllers (MFCs). Pressure control valves (PCVs) keep the pressure constant in the bubbler. The MOVPE reactor is a horizontal quartz (SiO₂) tube. The substrate for NW growth is put on a carbon susceptor, which is heated by a radio frequency (RF) coil in the reactor. The substrate temperature is monitored by a thermocouple inserted beneath the susceptor. The total gas flow rate in the reactor is maintained at 3.00 standard liters per minute (SLM). The working pressure is automatically kept at 0.1 atm, i.e., 76 Torr, by an automatic pressure controller (APC) and a vacuum pumping during the MOVPE growth. For the growth of the InAs NWs in this study, trimethylindium (TMIn) and 20%-arsine (AsH₃) diluted in H₂ are used for group-III MO source material and for group-V gas source, respectively. For the growth of MnAs nanoclusters (NCs), we use Bis(methyl- η^5 -cyclopentadienyl)manganese, namely, (MeCp)₂Mn or (CH₃C₅H₄)₂Mn.

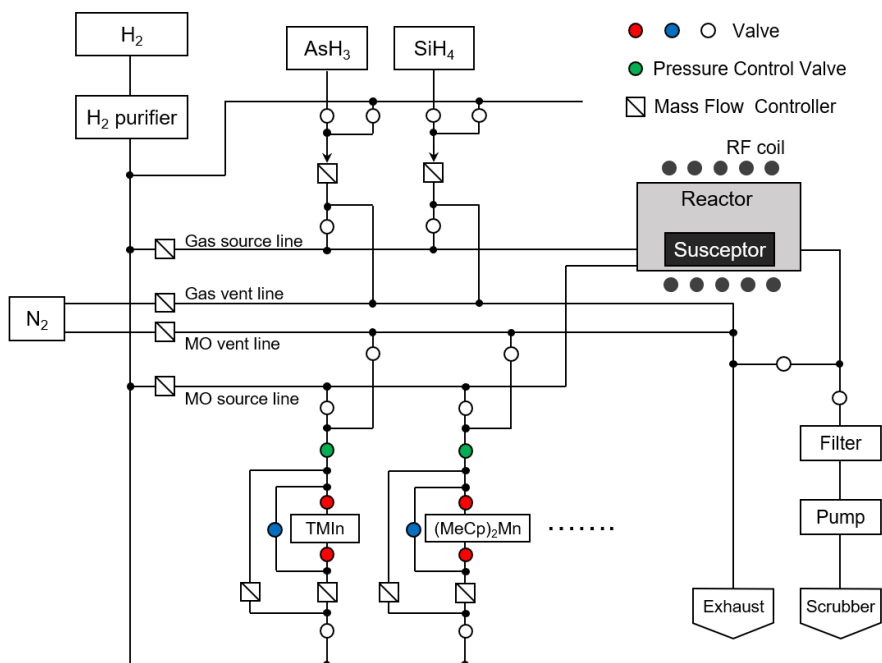


Figure 3-2. Schematic illustration of the MOVPE system used in this study. The horizontal reactor is maintained at working pressure of 0.1 atm and with a total flow of 3.00 SLM.

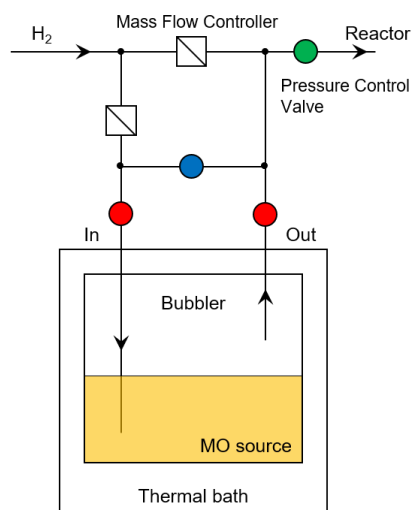


Figure 3-3. Schematic illustration of the lines of a MO source provided from a bubbler. When the MO source is used, the red (blue) valves are opened (closed).

3.3 Nanowire fabrication by selective-area MOVPE

The fabrication procedure of the substrates for the growth of vertical MnAs/InAs heterojunction NWs is as follows. First, SiO₂ thin films were deposited on the GaAs (111)B substrates by plasma sputtering system (Shibaura Mechatronics Corporation, CFS-4EP-LL). The thickness of SiO₂ thin films were estimated to be approximately 20 to 30 nm, which were measured by ellipsometry (ULVAC, ESM-1AT). After ultrasonic cleanings in acetone, ethanol, and ultrapure water for 5 min in each, an electron beam (EB) resist (Nippon Zeon: ZEP520A-7) was coated on the substrate by a spin-coater. The substrates were pre-baked at 170 °C for 2 min and 90 °C for 5 min, and then they were cooled to room temperature to prevent from surface cracks of the resist by a heat contraction. The EB lithography system (JEOL, JBX-6300SF) using a ZrO/W field emitter with an accelerating voltage of 100 kV is used for making periodical hexagonal opening patterns in the EB resist. After EB exposure, the substrates are developed with ZED-N50 solution for 90 sec, and rinsed with isopropanol solution for 60 sec. The substrates are then post-baked at 140 °C for 10 min and cooled at room temperature. Next, SiO₂ thin films within the periodical hexagonal opening formed in the EB resist were etched by reactive dry etching with CF₄, and the EB resist films are removed by methyl-ethyl-ketone (MEK). Before loading samples to the reactor, the substrates are cleaned with organic solvents in an ultrasonic bath, and the native oxide on the surface of the substrates are removed by alkali solution (Furuuchi Chemical, Semico Clean 23) for 10 min in an ultrasonic bath.

3.4 Lateral nanowire sample fabrication

The fabrication process of the lateral NW samples for the magnetization and magnetotransport characterizations of single NWs is as follows. First, the vertical free-standing NWs were detached from the GaAs (111)B substrates mechanically by ultrasonic vibration in isopropanol solution, and deposited on SiO₂/Si substrates. Before the deposition, metallic markers were formed on the SiO₂/Si substrates in order to determine the position of the NWs laid on SiO₂/Si substrates. Electrical contacts for the magnetotransport measurements were prepared on single NWs using electron-beam lithography followed by thermal evaporation of Ti/Au or Ti/Pd/Au thin layers. Just

before the metal evaporation, the electrical contact areas of NWs were treated with Semico Crean 23 solution or argon milling to etch off the native oxide on the NW surface.

3.5 Characterization

3.5.1 Scanning electron microscopy

Structural characterization of vertical free-standing NWs was carried out by secondary electron imaging by scanning electron microscopy (SEM) using Hitachi SU 8010. The accelerating voltage of 3 or 30 kV is mostly used in this study. The SEM system consists of an electron column with an electron source, condenser lenses, apertures, scanning coils, an objective lens and a specimen chamber. The column is kept at a high vacuum to prevent from an electrical discharge, to extend the lifetime of the electron gun, and to reduce undesirable collisions between electrons and air molecules. For the structural characterization of the lateral NW samples, the backscattered electron (BSE) imaging by the SEM was used because it is much more effective to distinguish the MnAs NCs from the host InAs NWs in and on the heterojunction NWs. The BSE imaging is sensitive to solid compositions of the observed materials since the BSE emission increases with increasing mean atomic number of materials [4]. The accelerating voltage of the electron beam was set to 1 kV for the BSE imaging in this study.

3.5.2 Magnetic force microscopy

We used magnetic force microscopy (MFM) combined with atomic force microscopy (AFM) in a Nanoscope IIIa system, Digital Instruments, mainly in the conventional phase detection (PD) mode of the system at room temperature and without any application of external magnetic fields, \mathbf{B} , during the observations. Before the MFM observations using a high-resolution-type MFM tip of Si coated with Co/Cr alloy materials (Bruker MESP-HR10), \mathbf{B} of 2 to 5.7 kG was applied to the lateral NW samples using a conventional stand-alone electromagnet. The coercivity of the MFM tip is 950 Oe according to the specification sheet published by Bruker AXS. To ensure that

we did not detect structural responses but magnetic ones from the MnAs NCs in the lateral NW samples, additional MFM observations were carried out using an MFM tip magnetized in the opposite direction or using amplitude detection (AD) mode of the MFM system. In the AD mode measurements, the resonance curve of the MFM cantilever is shifted when it is affected by stray magnetic fields. At the same time, the amplitude change of the MFM cantilever is detected at the point of drive frequency, which is set to be lower or higher than the resonance frequency of a free-vibrating MFM cantilever. The change in the MFM tip magnetization direction in the PD mode and the change in drive frequency in the AD mode give the reverse contrast of the magnetized regions in MFM images. We utilize the tapping mode in all MFM observations in this study.

3.5.3 Transport measurement system

For the magnetotransport characterizations of single undoped-InAs and MnAs/InAs heterojunction NWs in the lateral NW samples, we used the measurement system at Institute of Experimental Physics I, Justus Liebig University, Giessen, Germany [5]. It consists of an Oxford VTI-cryostat embedded in a superconducting magnet system yielding external magnetic fields up to 10 T. The sample was cooled with liquid helium, and the sample temperature can be adjusted between 1.6 and 280 K.

Bibliography

- [1] K. Ikejiri, “Growth Mechanism of III-V Semiconductor Nanowires by Selective Area Metalorganic Vapor Phase Epitaxy”, PhD Thesis, Hokkaido University, Japan (2013).
- [2] Y. Kohashi, “Growth Dynamics and Applications of Selectively-Grown InGaAs Nanowires”, PhD Thesis, Hokkaido University, Japan (2014).
- [3] G. B. Stringfellow, *Organometallic Vapor-Phase Epitaxy: Theory and Practice* (Academic Press, Inc.) second edition (1999).
- [4] E. Sánchez, M. T. Deluigi, G. Castellano, *Microsc. Microanal.* **18**, 1355 (2012).
- [5] M. Fischer, “Ordered arrangements of selective-area grown MnAs nanoclusters as components for novel, planar magneto-electronic devices”, PhD Thesis, Justus Liebig University, Germany (2015).

Chapter 4

Growth of Ferromagnetic MnAs/Semiconducting InAs Heterojunction Nanowires

The purpose of this chapter is to synthesize vertical ferromagnetic MnAs/semiconducting InAs heterojunction nanowires by combining the catalyst-free selective-area metal-organic vapor phase epitaxy of InAs nanowires and the endotaxial nanoclustering of MnAs. We report on a possible growth mechanism of MnAs nanoclusters in the vertical MnAs/InAs heterojunction nanowires on the basis of detailed structural characterization and growth condition dependence results. Size and shape of MnAs nanoclusters can be controlled by the growth temperature and time. The nanowire length and the surface migration length of manganese adatoms on the nanowires, which is estimated to be 600 nm at 580 °C, are the keys to the successful fabrication of vertical MnAs/InAs heterojunction nanowires with atomically abrupt heterointerfaces. The nanowire length and the surface migrations length are controlled by the distances between nanowires, or the period, and the growth temperature of MnAs nanoclusters, respectively. (This chapter is described mainly based on our previous studies [1, 2].)

4.1 Introduction

Vertical free-standing semiconducting nanowires (NWs) have recently been demonstrating extraordinary versatility and extremely high possibility for use in potential applications to next-generation electronic, photonic, sensing, and spintronic devices [3-15]. In recent semiconductor nanospintronic research fields, activities to achieve the heteroepitaxy of ferromagnetic layers and III-V compound semiconductors have attracted a great deal of attention owing to possible additional functionalities that have been added to current semiconducting devices and integrated circuits. Among these approaches, granular hybrid structures in which ferromagnetic nanoclusters

(NCs) are embedded into semiconductor layers are one of the most attractive candidate materials for future nanospintronic devices because they have been reported to have huge magnetoresistance effects and a relatively long spin-relaxation time [16-18]. We have, therefore, developed hybridization techniques of ferromagnetic MnAs NCs [19] on vertical free-standing semiconducting NW templates grown by our catalyst-free selective-area metal-organic vapor phase epitaxy (SA-MOVPE) technique [20, 21] in the research fields of semiconductor nanospintronics, and reported on the formation and characterizations of MnAs NC/GaAs hybrid NWs [22, 23]. However, we realized that it is still difficult to form vertical heterojunction NWs between ferromagnetic MnAs and semiconducting GaAs layers, which would enable us to inject spin-polarized carriers and currents into semiconducting NW channels. It is also difficult to control the crystal orientation of MnAs NCs in a $\langle 111 \rangle$ -oriented GaAs NW templates [22, 23] and to obtain atomically abrupt heterointerfaces between MnAs and GaAs even when using our hybridization techniques. On the other hand, we observed that MnAs NCs were grown much deeper into InAs NW templates and that the crystal orientation of MnAs NCs could be well-controlled in the InAs NWs [24]. These results indicate that the possibility of formation of vertical MnAs/InAs heterojunction NWs and the controllability of magnetizations of MnAs NCs in the vertical heterojunction NWs, which are advantage to create nanospintronic devices using vertical semiconducting NWs. Thus, we believe that the combination of a magnetic tunnel junction electrode and vertical ferromagnetic MnAs/semiconducting InAs heterojunction NWs with atomically abrupt heterointerfaces [25] could overcome major obstacles of conductance mismatch and poor controllability in the heterointerface formation in the current spin transistors [26]. In addition, the $\{111\}$ -oriented semiconducting NW channels possibly have a great advantage for enhancing spin lifetime in the channels of spin transistors [27].

Therefore, we report on the synthesis of high-quality vertical ferromagnetic MnAs/semiconducting InAs heterojunction NWs with atomically abrupt heterointerfaces utilizing the so-called endotaxy of MnAs NCs after the SA-MOVPE of InAs NW templates. A possible mechanism of the formation of single-crystal MnAs NCs was discussed on the basis of the detailed dependences of the MnAs NC formation on growth conditions and structural characterizations.

4.2 Experimental procedure

We used InAs NW arrays as a template, which were fabricated heteroepitaxially on GaAs (111)B substrates by utilizing the SA-MOVPE process, for creating high-quality vertical ferromagnetic MnAs NC/semiconducting InAs heterojunction NWs. First, we prepared the initial circular openings, which were arranged and defined in SiO₂ thin films by electron beam lithography. There were typically two types of the observed diameter d_0 of the initial circular openings: one was approximately 80 to 90 nm and the other was approximately 110 to 140 nm. The distances between the initial circular openings or the periods a were 0.5, 1.0, and 3.0 μm on the substrates. The SiO₂ thin films, whose typical thicknesses were estimated to be approximately 20 to 30 nm, were deposited on GaAs (111)B wafers by plasma sputtering. The growth temperature T_g and the growth time t for InAs NWs were 580 °C and 30 min, respectively. Conventional organometallic and hydride sources, such as (CH₃)₃In and 20%-AsH₃ diluted in H₂, were used as the group III sources for the former and group V sources for the latter in all the growth experiments. The estimated partial pressures of (CH₃)₃In [28] and 20%-AsH₃ diluted in H₂ were 4.9×10^{-7} and 1.3×10^{-4} atm, respectively, for the SA-MOVPE of undoped InAs NW templates. We utilized the phenomenon of the “endotaxy” of MnAs in InAs for MnAs NC growth after InAs NW growth. Endotaxy is associated with a diffusion process that leads to the redistribution of substances, i.e., MnAs NCs in host crystals, InAs NWs in the current work, and the formation of new stable phases. This is the key technique for forming ferromagnetic MnAs NCs “into” semiconducting NWs grown by SA-MOVPE. During the endotaxial growth of MnAs NCs into the host InAs NW templates, we only supplied the organometallic source of (CH₃C₅H₄)₂Mn diluted in H₂. The growth temperatures T_g for the MnAs NCs were changed from 400 to 580 °C, and their growth times t were changed from 1 to 5 min. The estimated partial pressure of (CH₃C₅H₄)₂Mn was 3.0×10^{-6} atm. During the decrease in temperature during the purging process after MnAs NC growth, 20%-AsH₃ diluted in H₂ was supplied. Structural characterizations in terms of the size and position of MnAs NCs and InAs NW templates were carried out by scanning electron microscopy (SEM). Transmission electron microscopy (TEM) was also used for obtaining lattice images of NCs and NWs, and we conducted detailed structural characterizations, such as the analyses of crystal structures and solid compositions of the NCs and NWs, by electron-beam diffraction (ED) and energy dispersive X-ray (EDX) spectroscopy in combination with TEM, using an electron beam with a spot diameter of about 1 nm.

4.3 Results and discussion

4.3.1 Structural characterizations

We first grew a template structure of InAs NW arrays on GaAs (111)B substrates by SA-MOVPE to fabricate vertical ferromagnetic MnAs NC/semiconducting InAs heterojunction NWs. Figure 4-1(a) shows a typical bird's-eye view obtained by SEM of the template structure of InAs NW arrays before the endotaxy of MnAs NCs. The period of InAs NWs, a , in Figure 4-1(a) was 1.0 μm . The diameter of the InAs NWs was estimated to be approximately 150 nm and their height was estimated to be approximately 1.5 μm , when we used the initial circular openings with the diameters, d_0 , of 110 to 140 nm in the SiO₂ thin films. We observed InAs NWs typically with a diameter of approximately 120 nm for the initial circular openings with the d_0 values of 80 to 90 nm from rough estimates. The inset in Figure 4-1(a) is a highly magnified top view SEM image of the InAs NWs. We observed that InAs NWs with a hexagonal prismatic shape were surrounded by six $\{0\bar{1}1\}$ crystal facets and grew in the $\langle 111 \rangle_B$ direction on GaAs (111)B substrates. The tops of the NWs revealed that flat $\{111\}_B$ crystal facets surrounded by tilted $\{-1\bar{1}0\}$ ones were formed. Figure 4-1(b) shows typical vertical MnAs/InAs heterojunction NWs grown at 580 °C for 1 min. The NCs were formed on the top $\{111\}_B$ crystal facets of the InAs NWs, and we also observed that some additional NCs were formed around the middle parts of the NWs.

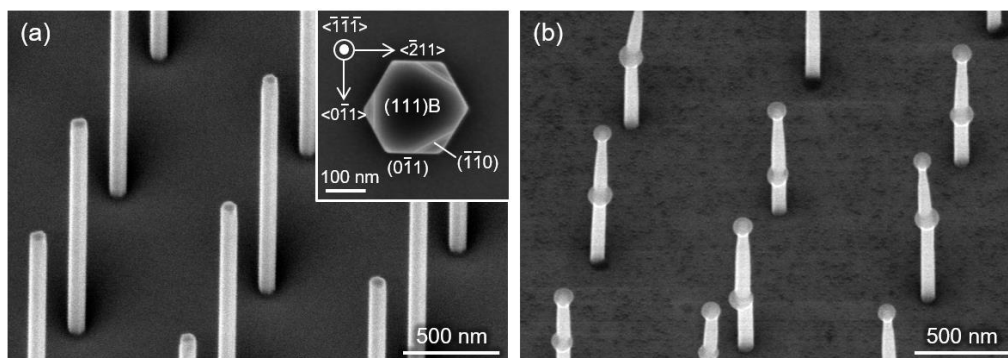


Figure 4-1. Bird's-eye view SEM images of typical (a) host InAs NW array template before the synthesis of MnAs NCs and (b) MnAs/InAs heterojunction NWs. Inset of (a) is a top view SEM image of crystal facets typically formed on top of host InAs NWs.

We next conducted structural characterizations by TEM for comparably similar heterojunction NWs to carefully investigate structural characteristics of the MnAs/InAs heterojunction NWs shown in Figure 4-1(b). Figures 4-2(a) and 4-2(b) show highly magnified cross-sectional bright-field TEM images of MnAs NCs that were formed in the middle and on the top $\{111\}$ B crystal facets of the host InAs NWs, respectively. The width and height of the NC in Figure 4-2(a) were estimated to be approximately 85 nm for the former and 55 nm for the latter, and those in Figure 4-2(b) were estimated to be approximately 72 nm for the former and 54 nm for the latter. We confirmed from TEM measurement results that rotational twin defects were randomly formed in the InAs NWs, and that no dislocations or defects, on the other hand, were observed in the MnAs NCs. We conducted EDX spectroscopy of the MnAs NCs formed in the middle and on the top $\{111\}$ B crystal facets of NWs in addition to the cross-sectional TEM observations, as shown in Figures 4-2(c) and 4-2(d), respectively. The atomic compositions of NCs and NWs in terms of three elements, i.e., arsenic, indium, and manganese, were estimated from the line profiles obtained by EDX spectroscopy. We eliminated possible external contamination by chemicals (or atoms), such as carbon, oxygen, and silicon, which were possibly introduced during the sample preparation processes and from the materials of the sample holders used for the TEM observations to precisely examine the solid compositions of NCs and NWs. The solid compositions (atomic compositions in %) of arsenic, indium, and manganese elements were estimated to correspond to approximately 52, 1, and 47% in the regions of the NC in Figure 4-2(c). We also concluded that the MnAs NCs that were formed on the top $\{111\}$ B crystal facets of the host InAs NWs had similar solid compositions, i.e., they corresponded to approximately 51, 0, and 49% of arsenic, indium, and manganese elements, as shown in Figure 4-2(d). Figures 4-2(e) and 4-2(f) show the ED pattern of the MnAs NC and a lattice image around the interface between the NW and the NC that were formed in the middle of NW, respectively. The ED pattern in Figure 4-2(e) revealed that the MnAs NC had a hexagonal NiAs-type crystal structure. The host InAs NWs, on the other hand, had a zinc-blende-type (ZB-type) crystal structure. The c-axes, i.e., the $\langle 0001 \rangle$ directions, of the NiAs-type MnAs NCs were approximately parallel to the $\langle 111 \rangle$ B directions of the host ZB-type InAs NWs. We confirmed that atomically abrupt heterointerfaces between MnAs NCs and InAs NWs were formed, as shown in Figure 4-2(f). Similar results in terms of the heterointerfaces were obtained for the NCs formed on the top $\{111\}$ B crystal facets of NWs. We concluded from these results of structural characterization that the vertical MnAs/InAs

heterojunction NWs with the atomically abrupt heterointerfaces were successfully formed by utilizing the endotaxy of MnAs NCs at the T_g of 580 °C.

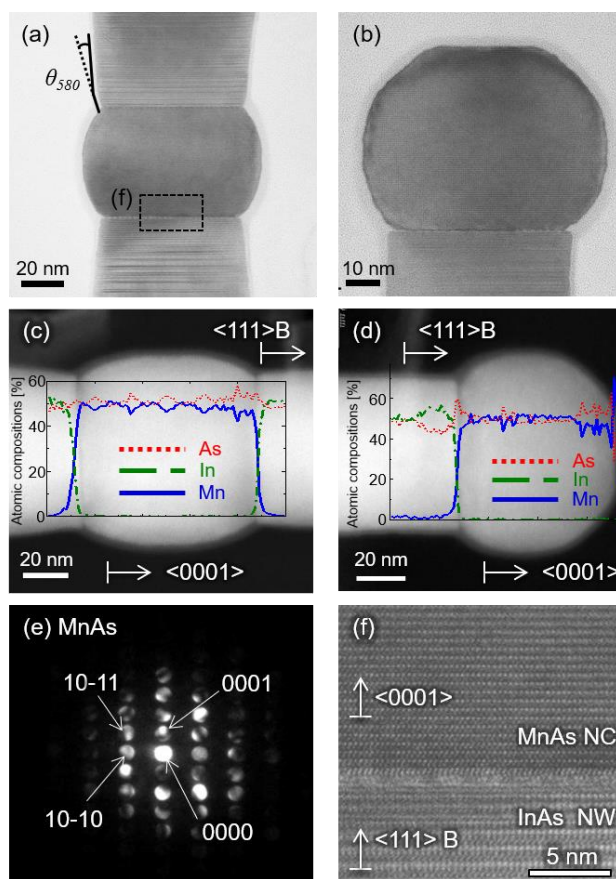


Figure 4-2. Cross-sectional TEM images of ferromagnetic MnAs NCs formed (a) in the middle and (b) on the top $\{111\}$ B crystal facet of semiconducting InAs NWs. MnAs NCs were grown at 580 °C for 1 min. Cross-sectional TEM images with corresponding line profile obtained by EDX spectroscopy for (c) middle and (d) top of NW. The percentages of arsenic, indium, and manganese elements were estimated by eliminating possible external contamination by chemicals (or atoms), such as carbon, oxygen, and silicon, which were possibly introduced during sample preparation processes and from materials of sample holders used for TEM observations. (e) Electron-beam diffraction pattern for MnAs NCs showing MnAs NCs with hexagonal NiAs-type crystal structure. (f) Lattice image of atomically abrupt heterointerface between InAs and MnAs layers that were formed in the middle of NW.

We also observed the endotaxial phenomenon of MnAs nanoclustering in the case of the MnAs NCs grown at 490 °C for 1 min, which was first reported in our previous paper [24]. The detailed TEM observations, ED measurements, and EDX spectroscopy in the current study revealed that the MnAs NCs were not only formed similarly on the top $\{111\}$ B crystal facets of the host InAs NWs, but also grew partially into the NWs from the $\{0-11\}$ sidewall crystal facets and/or six ridges between them (i.e., the MnAs NCs did not completely penetrate the NWs to form heterointerfaces within the cross-sectional NW areas), as shown in Figures 4-3(a) and 4-3(b). In the case of the NCs grown at 490 °C, some of the c-axes of MnAs NCs were not parallel to the $\langle 111 \rangle$ B directions of InAs NWs, as shown in Figure 4-3(b). We observed that the hexagonal

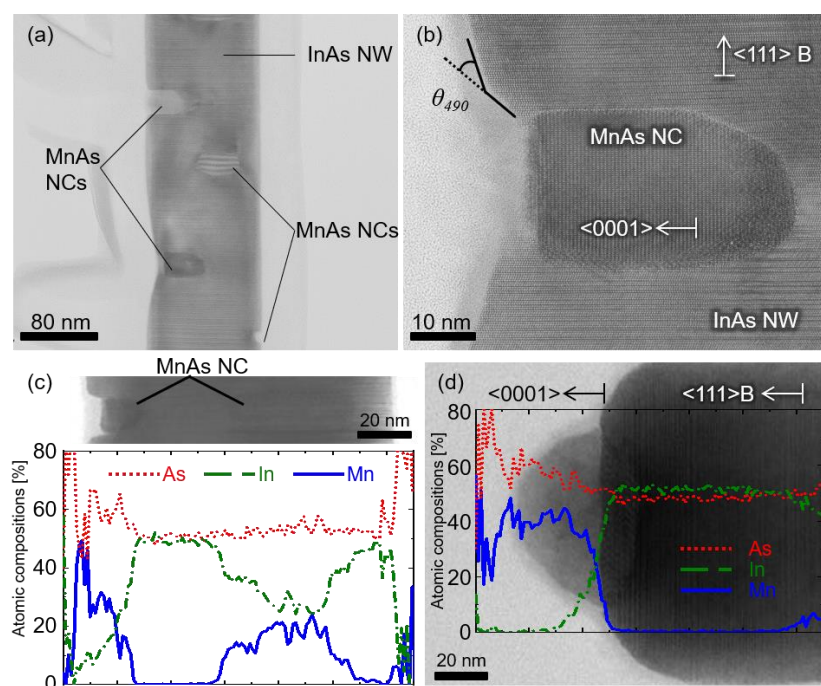


Figure 4-3. (a) Highly magnified cross-sectional TEM image of middle of vertical MnAs/InAs hybrid NWs in which MnAs NCs were grown at 490 °C for 1 min. (b) Lattice image for one of the MnAs NCs formed in the middle of the host InAs NW. Line profiles obtained by EDX spectroscopy for (c) middle and (d) top parts of the MnAs/InAs hybrid NW. The percentages of arsenic, indium, and manganese elements were estimated by eliminating possible external contamination by chemicals (or atoms), such as carbon, oxygen, and silicon.

truncated pyramidal shapes of the NCs formed on the top of host InAs NWs were rotated by 30° against the host NW hexagonal prisms. This was consistent with the results of our previous study [24]. We found that the MnAs NCs grown at 490 °C for 1 min, which were mainly composed of arsenic and manganese elements, had a hexagonal NiAs-type crystal structure, similarly to the NCs in Figure 4-2. However, in the MnAs NCs grown at 490 °C, small amounts of the indium element were observed even in the MnAs NC regions, as shown in Figures 4-3(c) and 4-3(d). This observation suggests two possibilities. One is that the indium elements of the InAs NWs behind the MnAs NCs were possibly detected in the NCs formed in the middle because the MnAs NCs did not completely penetrate the InAs NWs. The other is that InMnAs was grown during the synthesis of MnAs NCs. Neither of the possibilities can still be excluded in the current work.

4.3.2 Growth condition dependences and growth mechanism of MnAs nanoclusters

Some researchers have reported on the endotaxial nanoclustering of MnP in GaP(001) substrates [29]. The large diffusion coefficients of the interfacial diffusion of manganese atoms during the endotaxy of MnP in the GaP substrates are discussed in this article. The endotaxial depth of MnP NCs in the GaP substrates increased with increasing T_g for the MnP growth. We roughly estimated the depths of endotaxial MnAs nanoclustering, d , and the diffusion coefficients of manganese atoms, $D = d^2/4t$, from the TEM images of two types of NWs in which MnAs NCs were grown at 490 and 580 °C for 1 min. For the NWs with MnAs NCs grown at 490 °C, d and D were estimated to be 46 nm and 9 nm² s⁻¹, respectively. For the NWs with MnAs NCs grown at 580 °C, on the other hand, d and D were 83 nm and 28 nm² s⁻¹, respectively. The d and D increased with increasing T_g for MnAs NCs. Therefore, it was consistent with the experimental results reported previously [29]. In addition, the results suggest that the growth mechanism of the MnP/GaP system was similar to that proposed by W. Braun et al. for the growth of a MnSb film on GaSb [30]. The gallium atoms at the MnP/GaP interface were replaced by manganese atoms and diffused to the surface, and then such out-diffused gallium atoms combined with phosphorus atoms, which are present at the surface during the growth of MnP NCs. The substitution reaction from gallium to manganese atoms at the MnP/GaP interface is reasonable, because the standard

Table 4-1. The standard enthalpies for the formation reactions of the elements ΔH_f (kJ mol⁻¹) for MnP, GaP, MnAs, InAs, and GaAs at 700, 800, and 900 (K) [31].

	MnP	GaP	MnAs	InAs	GaAs
700 K	-114.728	-108.678	-47.094	-64.088	-81.582
800 K	-115.101	-108.909	-45.766	-64.622	-82.011
900 K	-115.564	-109.086	-44.523	-65.123	-82.430

enthalpies for the formation reactions of the elements, ΔH_f , at 900 K (approximately 630 °C) for MnP and GaP binary compounds are -115.564 and -109.086 kJ mol⁻¹, respectively as summarized in Table 4-1 [31], although N. Nateghi et al. did not discuss ΔH_f in their report [29]. However, it is somewhat difficult to expect the substitution reaction from indium to manganese atoms in our system, because ΔH_f at 800 K (approximately 530 °C) for MnAs and InAs are -45.766 and -64.622 kJ mol⁻¹, respectively [31]. This suggests that other growth mechanisms worked in our MnAs NC/InAs NW system. In addition, the tendency for MnAs NCs to grow much deeper into the InAs NWs compared to the GaAs NWs [28] can be explained by the different ΔH_f between InAs and GaAs because ΔH_f of GaAs is lower than ΔH_f of InAs as summarized in Table 4-1 [31].

We observed that the total volume of MnAs NCs in one InAs NW increased with increasing T_g . The increase in the total volume of MnAs NCs was roughly estimated from the obtained TEM images to be approximately 140 % by changing the T_g from 490 to 580 °C. In addition, the TEM and SEM measurement results revealed that the host InAs NW diameters in the vicinities of MnAs NCs tended to slightly and gradually decrease after the MnAs NC growth, compared with those around the middle of the NWs away from the MnAs NCs, as shown in Figures 4-2(a) and 4-3(b). Bending of NW sidewalls was observed in the vicinities of NCs. Here, we defined the bending angles of NW sidewalls, θ , and the θ values for the NCs grown at 580 and 490 °C were defined as θ_{580} and θ_{490} , respectively, as shown in Figures 4-2(a) and 4-3(b). We confirmed that θ_{580} was much shallower than θ_{490} , as estimated in Figures 4-2(a) and 4-3(b). It is reasonable because the desorption rate of indium and arsenic atoms should increase with increasing T_g . The indium and arsenic atoms in the host InAs NWs are easily desorbed during the endotaxy of MnAs NCs

because only $(\text{CH}_3\text{C}_5\text{H}_4)_2\text{Mn}$ and H_2 are supplied. When we supplied only H_2 at 490°C for 1 min immediately after the growth of the InAs NW templates grown at 580°C for 30 min, we actually observed the decrease in NW height after the H_2 treatment. Figure 4-4(a) and 4-4(b) show bird's-eye view SEM images of the InAs NW templates and the InAs NWs after the H_2 treatment. The decrease in NW height was estimated to be approximately 70%. A slight and negligible decrease in NW diameter was also observed. Therefore, we clearly observed that the indium and arsenic atoms were markedly desorbed from the host InAs NWs under the current synthesis conditions for MnAs NCs. Figure 4-5(a) shows the dependences of MnAs NC formation on the period a of the host InAs NWs. The MnAs NCs were grown at 580°C for 1 min in all the experiments. The average height of the host InAs NWs and vertical MnAs/InAs heterojunction NWs were estimated using 30 randomly chosen NWs observed in the SEM images. The decreases in NW height after the endotaxy of MnAs NCs were estimated to be approximately 30% at least. In addition, the differences in NW height between before and after the endotaxy of MnAs NCs were almost constant (approximately 30% at least) for all the periods a of 3.0, 1.0, and 0.5 μm , i.e., no significant dependence of the decreases on the periods a was observed. These results clearly indicated that the incorporation of manganese atoms, which reacted with arsenic atoms in the host InAs NWs, suppressed the desorption of arsenic and/or indium atoms from the host NWs. Therefore, it was highly possible that the decreases in the NW height were mainly caused by the desorption of indium and arsenic atoms from the host InAs NWs during the endotaxy of MnAs

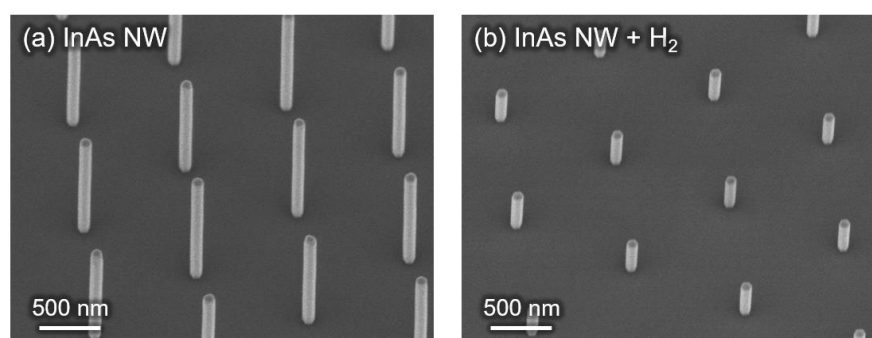


Figure 4-4. Bird's-eye view SEM images of (a) the InAs NW templates and (b) the InAs NWs after the H_2 treatment where we supplied only H_2 at 490°C for 1 min immediately after the growth of the InAs NW templates grown at 580°C for 30 min.

NCs. The results suggest that the desorption of indium and arsenic atoms from the host InAs NWs was a major trigger of the synthesis of MnAs NCs in the InAs NWs. Some of the desorbed arsenic atoms were incorporated into the solid phase after the chemical reactions with the supplied manganese atoms from the vapor phase. That resulted in the nucleation of MnAs on the NW surface. The synthesis of MnAs NCs proceeded “into” the host InAs NWs from the nuclei because of the following reasons. One is that the arsenic atoms in the host InAs NWs were consumed for the MnAs NC formation. Another reason is that the D of manganese atoms in the $\{111\}$ B plane was possibly larger than those in other planes since we observed that the crystal facets of the NCs and the MnAs/InAs heterointerfaces parallel to the InAs $\{111\}$ B plane were quite flat and abrupt compared with the other facets. Moreover, the penetration depth from the NW sides for almost all of the NCs was larger than these height in the $\langle 111 \rangle$ B direction of InAs NWs.

The insets in Figure 4-5(a) show that the host InAs NW height itself and the number of MnAs NCs formed in one NW decreased with the decreasing period a of the NWs. The decrease in NW height was possibly caused by the change in the amount of the indium source supplied per NW. The amount of indium source supplied per NW decreased with decreasing a because the surface migration length of indium atoms on the substrates was sufficiently larger than a . This resulted in the decrease in host InAs NW height at a relatively small a . This decrease in NW height led to the decrease in the number of NCs. The supplied manganese atoms were first adsorbed physically on the InAs NW surfaces after the diffusion from the vapor phase and then migrated on the surfaces. The manganese adatoms reached one of the possible chemical adsorption sites, where the indium and arsenic atoms presumably desorbed, and were then adsorbed chemically at vacant sites after indium and arsenic atoms had desorbed from the host InAs NWs. In the case of a small a , more of the manganese adatoms possibly reached one certain site because the surface migration length was sufficiently larger than the NW height. Therefore, the smaller the height of NWs, the fewer NCs were formed. In the case of a large a , on the other hand, the height of the host InAs NWs increased. A smaller number of manganese adatoms possibly reached one certain site because the surface migration length was not sufficiently larger than the NW height. This resulted in the growth of a large number of MnAs NCs in relatively long NWs. The inset in Figure 4-5(b) shows a typical bird’s-eye view SEM image of the vertical MnAs/InAs heterojunction NWs, in which several NCs were formed in the middle of NWs depending on the NW height. The MnAs

NWs were grown at 580 °C for 1 min. The NWs had a diameter of approximately 80 nm. We estimated the average heights of NWs as a function of the number of NCs formed in the middle of NWs from SEM images. As shown in Figure 4-5(b), the average height of NWs increased with increasing number of NCs. This suggests that the number of NCs was strongly affected by NW height and the surface migration length of manganese adatoms on the NW surface.

We next investigated the T_g dependences for the endotaxy of MnAs NCs. We measured the width of NCs formed on the top $\{111\}$ B crystal facets, W_{top} , and the vertical distance between the NCs, D_c , to carefully examine NC formation in and on the NWs for the NWs in which MnAs NCs were grown at 490, 540, and 580 °C. Figure 4-5(c) summarizes the T_g dependences of average W_{top} and D_c , which were estimated from 100 randomly chosen NWs observed in the SEM images, as shown in Figures 4-6(a) to 4-6(c). The inset in Figure 4-5(c) is a schematic that illustrates the definitions

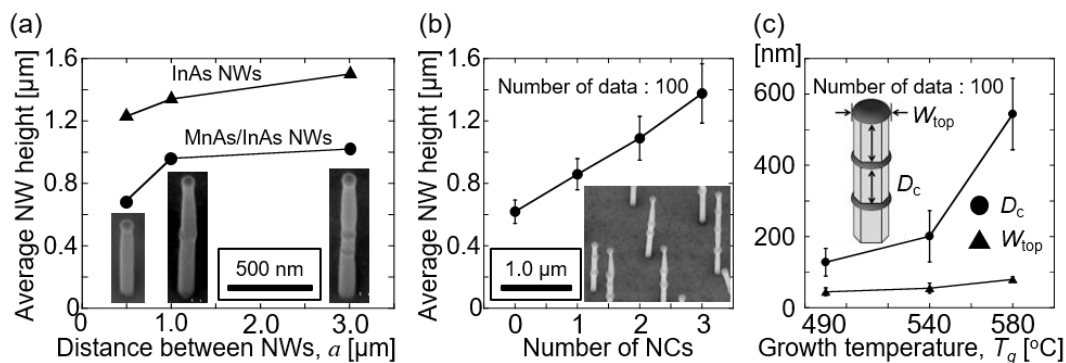


Figure 4-5. (a) Average height of host InAs NWs and vertical MnAs/InAs heterojunction NWs were estimated using 30 randomly chosen NWs observed in SEM images. They are plotted as a function of the host InAs NW periods a . Insets show bird's-eye view SEM images of vertical MnAs/InAs heterojunction NWs with a values of 0.5, 1.0, and 3.0 μm, in order from left to right. MnAs NCs were grown at 580 °C for 1 min by utilizing endotaxy. (b) The average height of NWs was estimated using 100 randomly chosen NWs observed in SEM images. They are plotted as a function of the number of MnAs NCs formed in the middle of NWs. Inset shows a bird's-eye view SEM image of vertical heterojunction NWs, which had MnAs NCs grown at 580 °C for 1 min. (c) The average size of MnAs NCs formed on top $\{111\}$ B crystal facets of host InAs NWs, W_{top} , and the distance between MnAs NCs, D_c , were estimated using 100 randomly chosen NWs. They are plotted as a function of growth temperatures T_g of NCs and are defined in the inset.

of W_{top} and D_c . Both W_{top} and D_c markedly increased with increasing T_g , as plotted in Figure 4-5(c). It was difficult to estimate D_c for the MnAs NCs grown at 400 °C for 1 min in the host InAs NWs because the NCs formed too closely to one another to identify as shown in Figure 4-6(d). However, we observed a tendency consistent with that observed in Figures 4-5(c). These experimental results suggest that the surface migration length of manganese adatoms on the sidewalls of the host InAs NWs is one of the key factors for the endotaxial formation of MnAs NCs. The larger the surface migration length became at higher T_g values, the larger the number of manganese adatoms that possibly reached one certain site. In addition, the desorption rates of indium and arsenic atoms and the D of manganese atoms increased at higher T_g values. These phenomena led to the increase in the size of NCs at a certain site and the decrease in the number of NCs. However, when the surface migration length decreased at lower T_g values, a small number of manganese adatoms possibly reached one certain site. The manganese adatoms in this case were possibly incorporated into other different sites within the range of their surface migration lengths. The desorption became less active and D became smaller at lower T_g values. As a result, it led to the decrease in the size of NCs and the increase in their number. Thus, the size and number of NCs were changed by T_g which affected the surface migration length of manganese adatoms,

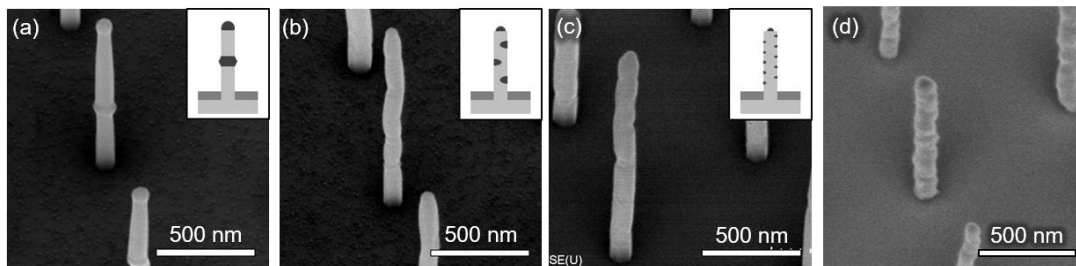


Figure 4-6. Bird's-eye view SEM images of vertical MnAs/InAs hybrid and heterojunction NWs in which MnAs NCs were grown at (a) 580, (b) 540, (c) 490, and (d) 400 °C for 1 min. Insets in (a) to (c) are schematics in which MnAs NCs are indicated by dark gray dots in and on bright gray InAs NWs. It was highly possible that the host InAs NWs in (d) was already lower than the other NWs in (a) to (c) before the NC formation. It was difficult to estimate the vertical distance between the MnAs NCs, D_c , for the NCs grown at 400 °C for 1 min in the host InAs NWs because the NCs formed too closely to one another to identify. However, we observed a tendency consistent with that obtained in Figure 4-5(c).

the desorption rate of indium and arsenic atoms, and the D of manganese atoms. The average height of NWs, at which no NC was formed in the middle, and the D_c obtained for the NCs grown at 580 °C were both approximately 600 nm, as shown in Figures 4-5(b) and 4-5(c). It was therefore possible for the surface migration length of manganese adatoms at a T_g of 580 °C to be roughly estimated from these results to be at least 600 nm. We concluded from these results that the period a of the host InAs NWs and T_g of MnAs NCs are the main factors for MnAs NC formation. At higher T_g values such as 580 °C, MnAs NCs penetrated the host InAs NWs with atomically abrupt heterointerfaces, as shown in Figure 4-2. Although the possibilities of the surface segregation of MnAs NCs and/or the merging among several NCs, which were reported elsewhere for a different-materials system [32], are not excluded, they might be low in the current study because no dislocations nor defects were observed in the MnAs NCs and because atomically abrupt heterointerfaces were formed between MnAs and InAs. Since rotational twin defects were randomly and densely formed in the host InAs NWs, there are supposed to be a large number of relatively unstable InAs bonds at the edges of atomic steps owing to the twin defects. These unstable InAs bonds at the edges can be the first sites for the nucleation of MnAs because the indium and arsenic atoms are easily desorbed there. Therefore, the difference between the densities of the twin defects might determine where the NCs are formed in the host NWs, although further experiments are required before we can conclude.

Finally, we investigated the growth times, t , dependences of MnAs NCs in the vertical MnAs/InAs heterojunction NWs, which successfully supported the possible growth mechanism of MnAs NCs suggested above. Figures 4-7(a) to 4-7(c) show bird's-eye view SEM images of the heterojunction NWs, in which MnAs NCs were grown at 580 °C for 1, 2, and 5 min, respectively. In all the cases, MnAs NCs were formed on the top $\{111\}$ B crystal facets and around the middle part of the host InAs NWs. Here, they are referred to as "top NCs" for the former and as "middle NCs" for the latter, as shown in Figure 4-7(a). The middle NCs completely penetrated the host InAs NWs with atomically-abrupt heterointerfaces between MnAs NCs and InAs NWs, and separated the host InAs NWs into upper and lower parts. Here, these upper and lower parts of InAs NWs are referred to as NW_{up} and NW_{low} , respectively, as shown in Figure 4-7(a). We observed from SEM images that the size of MnAs NCs increased with increasing t , while NW_{up} tended to be thinner and shorter than NW_{low} . The average height and width of both top and middle

NCs were estimated from 100 randomly chosen NWs observed in the SEM images. The average height and width of top NCs are defined here as H_{top} and W_{top} , and those of middle NCs are H_{mid} and W_{mid} , respectively. Figure 4-7(d) is a schematic that illustrates their definitions. We measured

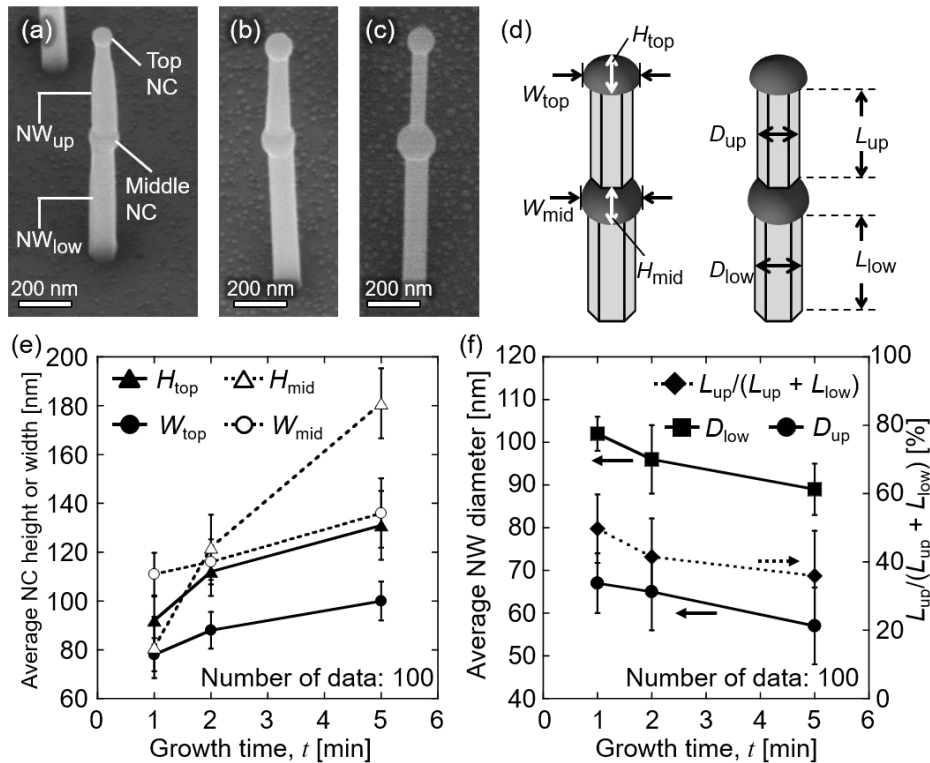


Figure 4-7. Bird's-eye view SEM images of vertical MnAs/InAs heterojunction NWs, in which MnAs NCs were grown at 580 °C for (a) 1, (b) 2, and (c) 5 min, respectively. (d) Schematic illustration for the definition of parameters used in Figures 4-7(e) and 4-7(f), H_{top} , H_{mid} , W_{top} , W_{mid} , L_{up} , L_{low} , D_{up} , and D_{low} . (e) Average height and width of MnAs NCs were estimated using 100 randomly chosen heterojunction NWs observed in SEM images. The average height and width of top NCs are defined as H_{top} and W_{top} , and those of middle NCs are H_{mid} and W_{mid} , respectively. They are plotted as a function of the growth time, t , of MnAs NCs. (f) Average length and diameter of InAs NWs were estimated using 100 randomly chosen heterojunction NWs observed in SEM images. The average length and diameter of an upper part of InAs NWs, NW_{up} , are defined as L_{up} and D_{up} , and those of a lower part of NWs, NW_{low} , are L_{low} and D_{low} , respectively. The D_{up} , D_{low} , and the percentage of L_{up} to the whole length of InAs NWs, i.e., $L_{\text{up}} + L_{\text{low}}$, are plotted as a function of the t of MnAs NCs. © 2017 The Japan Society of Applied Physics [2].

the maximum width at the middle parts of the NCs as W_{top} and W_{mid} . All the average height and width increased with increasing t , as plotted in Figure 4-7(e). Among them, we observed that H_{mid} drastically increased with increasing t . The average length and diameter of the NW_{up} and NW_{low} were also estimated from 100 randomly chosen NWs observed in the SEM images. The average length and diameter of NW_{up} are defined as L_{up} and D_{up} , and those of NW_{low} are L_{low} and D_{low} , respectively, as shown in Figure 4-7(d). We measured the diameter at the middle parts of the NWs as D_{up} and D_{low} . In Figures 4-7(a) to 4-7(c), the SEM images were taken from the samples tilted by approximately 45° . Here, therefore, H_{top} and H_{mid} for the NCs and L_{up} and L_{low} for the NWs are the values corrected by the tilt angle of 45° for all the observations. Both D_{up} and D_{low} decreased with increasing t , and L_{up} had also a tendency to decrease with increasing t compared to L_{low} , as plotted in Figure 4-7(f). These results suggest that arsenic atoms in the host InAs NWs were consumed as a source for the MnAs NC formation. This is consistent with the results as mentioned in the first part of this section. The middle NCs were located between NW_{up} and NW_{low} , in which InAs NWs acted as an arsenic source for the NC growth because we only supplied the manganese source diluted in H_2 . The top NCs, on the other hand, have only one interface with NW_{up} as an arsenic source. Therefore, the amount of arsenic supply for the middle NCs was larger than that for the top NCs. That resulted in the more drastic increase in H_{mid} compared to the other parameters, i.e., H_{top} , W_{top} , and W_{mid} . At the same time, for NW_{up} , the consumption of arsenic atoms occurs from both ends of the NW_{up} because NW_{up} was located between top and middle NCs. On the other hand, NW_{low} was consumed only by middle NCs. Thus, NW_{up} tended to be thinner and shorter compared to NW_{low} with increasing t . In addition, it is highly possible that the consumption of arsenic atoms began at much earlier stage in NW_{up} than NW_{low} as the top NCs were formed before the middle NCs. That resulted in the same tendency to be thinner and shorter in NW_{up} than NW_{low} . In our previous studies, the dependences of InAs and indium-rich InGaAs NW height on V/III ratio have been reported [33, 34]. The NW height monotonically decreased with decreasing the partial pressure of AsH_3 . Furthermore, we actually observed that the height of InAs NWs significantly decreased compared to their diameter, when we supplied only H_2 immediately after the InAs NW growth as shown in Figure 4-4. These results suggested that the desorption of indium and arsenic atoms from the top $\{111\}\text{B}$ crystal facet of NWs was enhanced by decreasing the partial pressure of AsH_3 . Thus, in this study, first, the supplied manganese atoms were incorporated with some of the arsenic atoms desorbed from the top $\{111\}\text{B}$ crystal facets to

form top NCs on the $\{111\}$ B crystal facet of NWs before middle NCs. During the NC growth, it was highly possible that arsenic and/or manganese atoms were desorbed to some extent even from MnAs NCs as well as InAs NWs because we supplied only manganese source diluted in H_2 . Therefore, that possibly led to the drastic increase in H_{mid} compared to H_{top} with increasing t , even though the top NCs were formed before the middle NCs. There was, in addition, a possibility that the desorption of arsenic and/or manganese atoms from the side-walls of middle NCs was larger than that from around the top and bottom heterointerfaces between middle NCs and InAs NWs because InAs NWs acting as an arsenic source for the NC growth were located on the top and bottom planes of middle NCs, i.e., the middle NCs were possibly elongated along the c -axis direction of NCs and the $\langle 111 \rangle$ B direction of NWs owing to the supply of arsenic atoms from the InAs NWs. That was a possible reason why the increase in W_{mid} was not as drastic as that in H_{mid} with increasing t .

4.4 Conclusions

We reported on the synthesis and structural characterizations of vertical MnAs/InAs heterojunction NWs by combining the SA-MOVPE of InAs NWs and the endotaxial nanoclustering of MnAs NCs. The c -axes, i.e., the $\langle 0001 \rangle$ directions, of the hexagonal NiAs-type MnAs NCs were approximately parallel to the $\langle 111 \rangle$ B directions of the host ZB-type InAs NWs in the heterojunction NWs with the atomically abrupt heterointerfaces. The detailed growth condition dependences revealed that the parameters T_g and a are the key factors for the formation of MnAs NCs into InAs NWs. The diffusion coefficients of manganese atoms, D , the surface migration length of manganese adatoms on the host InAs NWs, and the desorption rates of indium and arsenic atoms in the NWs strongly depended on the growth temperature T_g , and NW height changed according to the period of the host InAs NWs, a . At a relatively low T_g of 490 °C, the D , surface migration length, and desorption rate decreased. This led to a relatively large number of small MnAs NCs, which were shallowly formed into the NWs from the $\{0-11\}$ sidewalls. When T_g increased, on the other hand, the D , surface migration length, and desorption rate increased. This resulted in relatively large NCs that formed deeply into the host NWs and the decrease in

the number of NCs. At a T_g of 580 °C, the MnAs NCs penetrated the host InAs NWs. This phenomenon successfully led to the formation of vertical MnAs/InAs heterojunction NWs with atomically abrupt heterointerfaces between MnAs and InAs layers. The results of growth time t dependence also successfully supported the possible growth mechanism, which suggested that the arsenic atoms in the host InAs NWs were consumed for the MnAs NC formation. The size of MnAs NCs increased with increasing t of MnAs NCs. Among them, H_{mid} drastically increased compared to H_{top} , W_{top} , and W_{mid} , and NW_{up} tended to be thinner and shorter compared to NW_{low} with increasing t . Therefore, it would be possible to control the size and shape of MnAs NCs in vertical MnAs/InAs heterojunction NWs by changing the parameter t as well as T_g . We believe that our vertical MnAs/InAs heterojunction NWs in the current work have demonstrated new possibilities and versatility for creating future novel magneto-nanoelectronic or nanospintronic NW devices, e.g., spin-NW-transistors and spin-NW-light-emitting diodes, as was reported and discussed in our review paper [35].

Bibliography

- [1] R. Kodaira, S. Hara, K. Kabamoto, and H. Fujimagari, *Jpn. J. Appl. Phys.* **55**, 075503 (2016).
- [2] R. Kodaira, K. Kabamoto, and S. Hara, *Jpn. J. Appl. Phys.* **56**, 06GH03 (2017).
- [3] X. Duan, Y. Huang, Y. Cui, J. Wang, and C. M. Lieber, *Nature* **409**, 66 (2001).
- [4] J. Wang, M. S. Gudiksen, X. Duan, Y. Cui, and C. M. Lieber, *Science* **293**, 1455 (2001).
- [5] Y. Cui and C. M. Lieber, *Science* **291**, 851 (2001).
- [6] C. Thelander, T. Matensson, M. T. Björk, B. J. Ohlsson, M. W. Larsson, L. R. Wallenberg, and L. Samuelson, *Appl. Phys. Lett.* **83**, 2052 (2003).
- [7] X. Duan, Y. Huang, R. Agarwal, and C. M. Lieber, *Nature* **421**, 241 (2003).
- [8] D. Zhang, C. Li, X. Liu, S. Han, T. Tang, and C. Zhou, *Appl. Phys. Lett.* **83**, 1845 (2003).
- [9] P. Offermans, M. Crego-Calama, and S. H. Brongersma, *Nano Lett.* **10**, 2412 (2010).
- [10] B. Tian, X. Zheng, T. J. Kempa, Y. Fang, N. Yu, G. Yu, J. Huang, and C. M. Lieber, *Nature* **449**, 885 (2007).
- [11] J. Wallentin, N. Anttu, D. Asoli, M. Huffman, I. Åberg, M. H. Magnusson, G. Siefert, P. Fuss-Kailuweit, F. Dimroth, B. Witzigmann, H. Q. Xu, L. Samuelson, K. Deppert, and M. T. Borgström, *Science* **339**, 1057 (2013).
- [12] N. Han, F. Wang, J. J. Hou, S. P. Yip, H. Lin, F. Xiu, M. Fang, Z. Yang, X. Shi, G. Dong, T. F. Hung, and J. C. Ho, *Adv. Mater.* **25**, 4445 (2013).
- [13] Y. J. Hong, J. W. Yang, W. H. Lee, R. S. Ruoff, K. S. Kim, and T. Fukui, *Adv. Mater.* **25**, 6847 (2013).
- [14] P. Ren, W. Hu, Q. Zhang, X. Zhu, X. Zhuang, L. Ma, X. Fan, H. Zhou, L. Liao, X. Duan, and A. Pan, *Adv. Mater.* **26**, 7444 (2014).
- [15] J. Hubmann, B. Bauer, H. S. Körner, S. Furthmeier, M. Buchner, G. Bayreuther, F. Dirnberger, D. Schuh, C. H. Back, J. Zweck, E. Reiger, D. Bougeard, Epitaxial growth of room-temperature ferromagnetic MnAs segments on GaAs nanowires via sequential crystallization, *Nano Lett.* **16**, 900 (2016).
- [16] P. N. Hai, S. Ohya, M. Tanaka, S. E. Barnes, and S. Maekawa, *Nature* **458**, 489 (2009).
- [17] P. N. Hai, S. Ohya, and M. Tanaka, *Nat. Nanotechnology* **5**, 593 (2010).
- [18] M. Tanaka, S. Ohya, and P. N. Hai, *Appl. Phys. Rev.* **1**, 011102 (2014).
- [19] S. Hara, D. Kawamura, H. Iguchi, J. Motohisa, and T. Fukui, *J. Cryst. Growth* **310**, 2390 (2008).

- [20] T. Sato, Y. Kobayashi, J. Motohisa, S. Hara, and T. Fukui, *J. Cryst. Growth* **310**, 5111 (2008).
- [21] K. Tomioka, J. Motohisa, S. Hara, and T. Fukui, *Nano Lett.* **8**, 3475 (2008).
- [22] M. Yatago, H. Iguchi, S. Sakita, and S. Hara, *Jpn. J. Appl. Phys.* **51**, 02BH01 (2012).
- [23] S. Hara, S. Sakita, and M. Yatago, *Jpn. J. Appl. Phys.* **51**, 11PE01 (2012).
- [24] S. Hara, H. Fujimagari, S. Sakita, and M. Yatago, *Proc. SPIE* **8820**, 88200V (2013).
- [25] J. Tang, C.-Y. Wang, M.-H. Hung, X. Jiang, L.-T. Chang, L. He, P.-H. Liu, H.-J. Yang, H.-Y. Tuan, L.-J. Chen, and K.-L. Wang, *ACS Nano* **6**, 5710 (2012).
- [26] S. Sugahara and J. Nitta, *Proc. IEEE* **98**, 2124 (2010).
- [27] K. Biermann, A. Hernández-Mínguez, R. Hey, and P. V. Santos, *J. Appl. Phys.* **112**, 083913 (2012).
- [28] D. V. Shenai-Khatkhate, R. L. DiCarlo Jr., R. A. Ware, *J. Cryst. Growth* **310**, 2395 (2008).
D. V. Shenai-Khatkhate *et al.* reported on an update on the vapor pressure (P) equation of $(\text{CH}_3)_3\text{In}$, i.e., $\log P$ (Torr) = 10.98 - 3204/T (K). In the current work, however, we used the estimated partial pressure for $(\text{CH}_3)_3\text{In}$ obtained using a conventionally used old equation, i.e., $\log P$ (Torr) = 10.52 - 3014/T (K), for comparison with our previous papers.
- [29] N. Nateghi, D. Ménard, and R. A. Masut, *J. Appl. Phys.* **116**, 133512 (2014).
- [30] W. Braun, A. Trampert, V. M. Kaganaer, B. Jenichen, D. K. Satapathy, and K. H. Ploog, *J. Cryst. Growth* **301-302**, 50 (2007).
- [31] I. Barin, *Thermochemical Data of Pure Substances* (Wiley-VCH, Weinheim, 1989).
- [32] S. Hara and A. Kuramata, *Nanotechnology* **16**, 957 (2005).
- [33] K. Tomioka, P. Mohan, J. Noborisaka, S. Hara, J. Motohisa, and T. Fukui, *J. Cryst. Growth* **298**, 644 (2007).
- [34] Y. Kohashi, S. Hara, and J. Motohisa, *Mater. Res. Express* **1**, 015036 (2014).
- [35] M. T. Elm and S. Hara, *Adv. Mater.* **26**, 8079 (2014).

Chapter 5

Magnetization Characterization of MnAs Nanoclusters in Heterojunction Nanowires

We report on the magnetization and magnetic domains of ferromagnetic MnAs nanoclusters in MnAs/InAs heterojunction nanowires on the basis of the structural and magnetic characterization results. MnAs nanoclusters have single magnetic domains, and their magnetization is normally oriented along one of the a-axes, i.e., the magnetic easy axes of hexagonal NiAs-type MnAs, which are parallel to an applied external magnetic field. We occasionally observe the MnAs nanocluster magnetized along the c-axis, i.e., the magnetic hard axis, due to a shape anisotropy and the MnAs nanocluster with small coercivity in a markedly bended heterojunction nanowire. (This chapter is described mainly based on our previous studies [1-3].)

5.1 Introduction

Vertical semiconducting nanowires (NWs) are recently of great interest owing to their potential for applications in next-generation electronic, photonic, sensing, and spintronic devices [4-9]. For example, practical ways of integrating vertical surrounding gate field-effect transistors (FETs) using NWs to current integrated circuits based on CMOS technologies have been extensively demonstrated for future electronic industry using these NWs. In the nanospintronic research fields, heteroepitaxial structures between magnetic and III-V compound semiconducting materials have attracted much attention for future nanospintronic devices, such as spin-transistors [10-12]. We have developed a combined technique of catalyst-free selective-area metal-organic vapor phase epitaxy (SA-MOVPE) of vertical semiconducting InAs NWs and endotaxy of ferromagnetic MnAs nanoclusters (NCs) as described in Chapter 4 to create novel nanospintronic devices using vertical semiconducting NW channels, such as spin-NW-transistors. It is crucial to control the magnetization characteristics of MnAs NCs in the heterojunction NWs towards the creation of

NW spintronic devices, which are based on our vertical surrounding gate FET structures [6].

In this chapter, therefore, we report on the magnetization and magnetic domains of ferromagnetic MnAs NCs in MnAs/InAs heterojunction NW on the basis of the structural and magnetization characterization results obtained from scanning electron and magnetic force microscopies.

5.2 Experimental procedure

Vertical MnAs/InAs heterojunction NWs were fabricated heteroepitaxially on GaAs (111)B substrates by the endotaxy of MnAs NCs following the SA-MOVPE of periodical InAs NW array templates. The detailed fabrication procedures and growth conditions were given and explained in Chapter 4. MnAs NCs were grown at 580 °C for 1 or 2 min in this study. Structural characterizations in terms of the size and shape of MnAs NCs and MnAs/InAs heterojunction NWs were carried out by secondary and backscattered electron (BSE) imaging using a scanning electron microscope, SU8010 system, Hitachi. For the magnetization and further structural characterizations of ferromagnetic MnAs NCs in MnAs/InAs heterojunction NWs, we used magnetic force microscopy (MFM) combined with atomic force microscopy (AFM) in a Nanoscope IIIa system, Digital Instruments, mainly in the conventional phase detection (PD) mode of the system at room temperature and without any application of external magnetic fields \mathbf{B} during the observations. To ensure that magnetic responses from MnAs NCs were observed, we also conducted amplitude detection (AD) mode measurements in the MFM system. In the AD mode measurements, the resonance curve of the MFM cantilever is shifted when it is affected by stray magnetic fields from MnAs NCs. At the same time, the amplitude change of the MFM cantilever is detected at the point of drive frequency, which is set to be lower or higher than the resonance frequency of a free-vibrating MFM cantilever. The change in drive frequency gives the reversals in contrasts of the magnetized region in MFM images. For these observations, vertical MnAs/InAs heterojunction NWs were separated from GaAs (111)B substrates mechanically by ultrasonic vibration in isopropanol solution, and deposited on SiO₂/Si substrates. Before the MFM observations using a high-resolution-type MFM tip of Si coated with Co/Cr alloy materials, Bruker MESP-HR10, \mathbf{B} of 2 to 5.7 kG was applied to the heterojunction NWs laid on SiO₂/Si substrates using a conventional stand-alone electromagnet. The coercivity of the MFM tip used is 950 Oe according to the specification sheet published by Bruker AXS.

5.3 Results and discussion

5.3.1 MnAs nanoclusters magnetized along a-axes

Figures 5-1(a) and 5-1(b) show a secondary electron image and corresponding MFM images with the PD mode of the MnAs/InAs heterojunction NWs laid on the SiO₂/Si substrate, respectively. The MnAs NCs were grown at 580 °C for 1 min. It was quite difficult to examine the same heterojunction NW observed by transmission electron microscopy (TEM) in Chapter 4 using MFM since a large number of NWs were formed at the same time on the same GaAs (111)B substrate with various types of SiO₂-mask openings, i.e., different diameters of initial circular openings and distance between them. However, it was highly possible, as determined from the secondary electron image in Figure 5-1(a) and the structural characterization results shown in Chapter 4, that most of the MnAs NCs penetrated the host InAs NWs. It was likely in this case, therefore, that the c-axes of the hexagonal NiAs-type MnAs NCs were parallel to the $\langle 111 \rangle_B$ direction of the host zinc-blende-type (ZB-type) InAs NW (i.e., the magnetic easy axes, i.e., a-axes, of the NCs were perpendicular to the $\langle 111 \rangle_B$ direction of the NW). MnAs NCs “I” and “II” had a marked single magnetic domain after application of \mathbf{B} of 5.7 kG perpendicular to the substrate surface, as shown in Figure 5-1(b). Bright and dark contrasts were obtained in the regions of NCs I and II in the MFM images when the magnetized MFM tips detected repulsive and attractive forces from the stray magnetic fields from NCs in the heterojunction NW, respectively. For the NCs I and II, dark regions were observed at the center of the NC, and the bright regions were observed around the dark regions. It was revealed that the magnetized direction of the NCs I and II was possibly along one of the a-axes, which were presumably parallel to the applied \mathbf{B} direction. To ensure that the detected dark and bright contrasts in the images were due to magnetic responses, we also conducted MFM measurements for the NCs I and II in the AD mode, as shown in Figures 5-1(c) to 5-1(f). The drive frequencies were set higher in Figures 5-1(c) and 5-1(e), and lower in Figures 5-1(d) and 5-1(f) than the resonance frequency of a free-vibrating MFM cantilever. It was revealed that changing the drive frequency resulted in reversal contrasts in the regions of NCs I and II, which showed magnetic responses from the NCs. Therefore, we concluded that MnAs NCs I and II had a marked single magnetic domain and the magnetized direction of the NCs I and II was possibly along one of the a-axes, which were presumably parallel to the applied \mathbf{B} direction. Some articles, in addition, reported on the

magnetization and magnetic domain characterization results of MnAs NCs on conventional VLS-grown semiconducting NWs using MFM imaging at room temperature. Both of the reported MnAs NCs, which were deposited on the side-walls of InAs NWs [13] and only on the top surfaces of GaAs NWs [9], had marked single magnetic domains and were magnetized perpendicular to the *c*-axis of hexagonal NiAs-type MnAs NCs. Therefore, the magnetization directions observed in Figure 5-1 were consistent with the results reported in the articles by D. G. Ramlan *et al.* [13] and J. Hubmann *et al.* [9]. We have not determined the Curie temperature T_c of the MnAs NCs in InAs NWs. However, the hysteresis curves [14] and the increased T_c of 340 K [15] were observed for the comparable samples of NiAs-type MnAs NCs on InGaAs layers in our previous studies. Some researchers have reported on a single magnetic domain of MnAs that was epitaxially grown on GaAs NWs and observed the hysteresis curve of the MnAs and temperature-dependent curves, which revealed the T_c of MnAs on GaAs NWs to be 313 K [9].

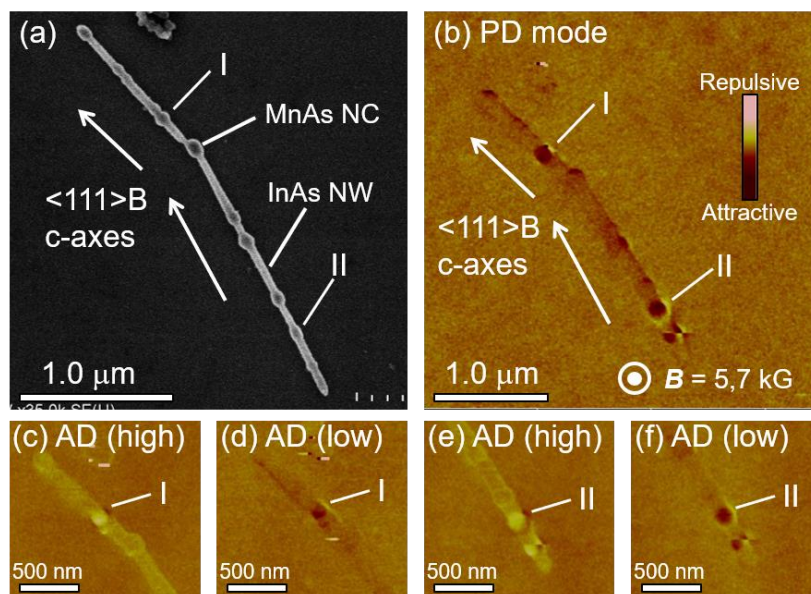


Figure 5-1. (a) A top view secondary electron image and (b) a corresponding MFM image of one of MnAs/InAs heterojunction NWs. The MFM image was observed in the conventional PD mode of the MFM system. (c)–(f) Highly magnified MFM images of NCs I and II, which were observed in the AD mode of the MFM system. (c, e) High and (d, f) low drive frequencies were set in the AD mode measurements. The reversals in contrasts of NCs I and II by changing the drive frequency clearly showed that magnetic responses were obtained from them.

5.3.2 MnAs nanoclusters magnetized along c-axis

Subsequently, we conducted MFM observations in the PD mode for another MnAs/InAs heterojunction NWs. Figure 5-2(a) shows BSE images of the observed NW, and the inset is a highly-magnified view of NC “III”. We observed in the image the multiple bright and dark regions in the MnAs/InAs heterojunction NW. Since the BSE emission increases with increasing mean atomic number of materials [16], these bright and dark regions corresponded to InAs NWs and MnAs NCs, respectively. The mean atomic number of InAs is larger than that of MnAs in the current work. It seemed that the heterointerfaces between MnAs and InAs were quite abrupt, as shown in Figure 5-2(a), which meant that the change in solid composition at the interfaces was quite abrupt. Therefore, it was highly possible that the hexagonal NiAs-type MnAs NCs penetrated the host ZB-type InAs NWs with atomically-abrupt heterointerfaces, and that the c-axes of MnAs NCs were approximately parallel to the $\langle 111 \rangle_B$ directions of the InAs NWs, judging from the structural characterization results reported in Chapter 4, in which the detailed structural characterizations were carried out for comparable similar heterojunction NWs by TEM. In this case, the a-axes, i.e., magnetic easy axes, of MnAs NCs were perpendicular to the $\langle 111 \rangle_B$ direction of InAs NW. The c-axis of NC III might be approximately parallel to the $\langle 111 \rangle_B$ directions of the upper or lower part of InAs NWs because the $\langle 111 \rangle_B$ directions of NWs were tilted (approximately 18°) at the position of NC III. Figure 5-2(b) shows the corresponding MFM image obtained at room temperature after the application of \mathbf{B} of 2 kG nearly parallel to the c-axis of NC III. As shown in the NC III in Figure 5-2(b), bright and dark areas were markedly observed within the NC III region, and the bright-dark contrast series aligned parallel to the c-axis of NC III. To ensure that the detected dark and bright contrasts were due to magnetic responses, we next conducted MFM observations using an MFM tip magnetized in the opposite direction from the direction used in Figure 5-2(b). As shown in Figure 5-2(c), the bright-dark contrast series in Figure 5-2(b) was reversed to the dark-bright contrast in the image depending on the magnetized direction of the MFM tip. The results, therefore, confirmed that the bright and dark contrasts observed within the NC III region were due to magnetic responses from the NC III. Thin white arrows represent possible magnetization directions, \mathbf{M} , of NC III, as shown in Figures 5-2(b) and 5-2(c). We subsequently observed an MFM image for the same NW after applying the \mathbf{B} of 2 kG in the opposite direction from the \mathbf{B} -direction applied in Figures 5-2(b) and 5-2(c). As shown in Figure 5-2(d), the NC III was possibly magnetized in the opposite direction from the \mathbf{M}

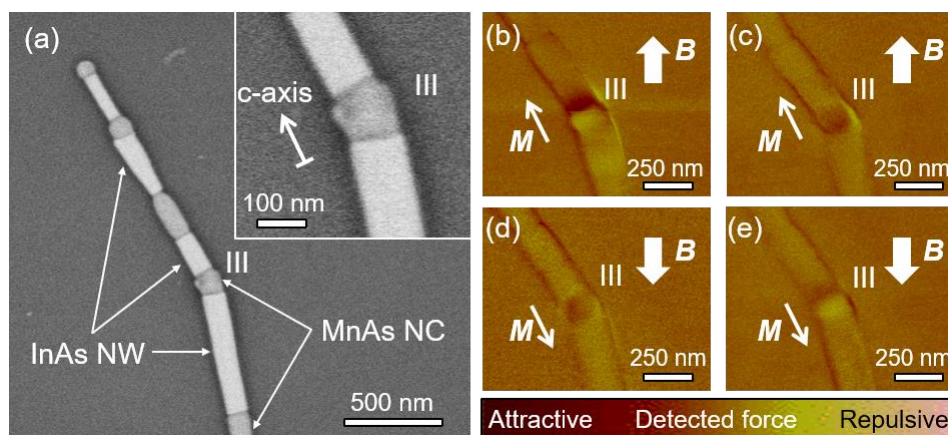


Figure 5-2. (a) A top view BSE image of the MnAs/InAs heterojunction NWs. Inset of (a) is a highly magnified BSE image of NC III with a relatively large height and aspect ratio R , which is defined as $R = \text{NC's height}/\text{NC's width}$, of approximately 1.1. (b)-(e) Corresponding highly magnified MFM images of NC III at room temperature. External magnetic fields \mathbf{B} of 2 kG were applied in the directions indicated by the thick white arrows in the figures. MFM images of (c) and (e), in particular, were taken with a reversely-magnetized MFM tip, i.e., the magnetized direction of MFM tip opposite to that used in (b) and (d), respectively, to ensure that the obtained dark-bright contrast series observed in the NC III region was due to the magnetic responses from the NC III. Thin white arrows indicate the possible magnetization directions \mathbf{M} of the NC III.

in Figures 5-2(b) and 5-2(c), depending on the \mathbf{B} -direction. To ensure that the result was due to magnetic responses, we also conducted MFM observations using an MFM tip magnetized in the opposite direction from the direction used in Figure 5-2(d), as shown in Figure 5-2(e). As reported in section 5.3.1, when we applied \mathbf{B} perpendicular to the $\langle 111 \rangle_B$ direction of NWs (i.e., parallel to one of the magnetic easy axes, a-axes, of MnAs NCs), we confirmed that the NCs were magnetized along one of the a-axes, which was parallel to the \mathbf{B} -direction. On the other hand, the NC III in Figures 5-2(b) to 5-2(e) in the current study showed different results, i.e., indicating that the NC III was possibly magnetized parallel to its c-axis. However, the c-axis of NiAs-type MnAs NCs is not the magnetic easy axis. Therefore, it appeared that the NC III was magnetized parallel to the c-axis possibly owing to the magnetic shape anisotropy of NC III with a relatively large height along the c-axis. Magnetization along the c-axis of MnAs NCs in the heterojunction NWs and its dependence on the shape of NCs were reported in detail in our previous study [17]. To

magnetize the MnAs NCs along the a-axes of the NCs, it may be necessary to decrease the aspect ratio of the NCs, R , which are defined as $R = \text{NC's height}/\text{NC's width}$, to approximately 0.80 or less. The R of NC III was estimated to be approximately 1.1 from the BSE image in Figure 5-2(a). Thus, the NC III was possibly magnetized along its c-axis, and it was consistent with the results and discussion in our previous report [17]. These results showed the possibilities that the magnetization direction of MnAs NCs can be controlled by the size and shape of NCs, which depend on mainly the growth time t of MnAs NCs because NC's height drastically increased with increasing t compared to NC's width as described in Chapter 4.

5.3.3 Magnetization in bended heterojunction nanowires

Finally, we investigated the magnetization of MnAs NCs located at relatively close range in a bended MnAs/InAs heterojunction NW, which were occasionally observed in the NWs with multiple MnAs NCs. The MnAs NCs were grown at 580 °C for 2 min. First, structural characterizations were carried out using BSE imaging for the MnAs/InAs heterojunction NWs laid on SiO₂/Si substrates. Figure 5-3(a) shows a top view BSE image for a bended MnAs/InAs heterojunction NW with multiple MnAs NCs. The bright and dark regions corresponded to InAs NWs and MnAs NCs, respectively, as explained in section 5.3.2. It was highly possible that MnAs NCs penetrated the host InAs NWs with atomically-abrupt heterointerfaces, and that the c-axes of MnAs NCs were approximately parallel to the $\langle 111 \rangle_B$ directions of the InAs NWs, judging from the BSE image in Figure 5-3(a) and the structural characterization results reported in Chapter 4. In this case, the a-axes, i.e., magnetic easy axes, of MnAs NCs were perpendicular to the $\langle 111 \rangle_B$ direction of InAs NWs. In Figure 5-3(a), the $\langle 111 \rangle_B$ direction of the middle part of InAs NW between NCs "IV" and "V" is defined as $\langle 111 \rangle_{B_{IV-V}}$, and the upper and lower parts of InAs NWs are referred to as $\langle 111 \rangle_{B_{IV}}$ and $\langle 111 \rangle_{B_V}$, respectively. Although no further information of crystallographic relations between NC V and $\langle 111 \rangle_{B_{IV-V}}$ or $\langle 111 \rangle_{B_V}$ in Figure 5-3(a), it may be possible that the c-axis of NC V is parallel to $\langle 111 \rangle_{B_{IV-V}}$ or $\langle 111 \rangle_{B_V}$ since the MnAs/InAs heterojunction NW is markedly bended at the position of NC V. The tilt angle of $\langle 111 \rangle_{B_{IV-V}}$ from $\langle 111 \rangle_{B_V}$ at the position of NC V is measured to be approximately 27°. On the other hand, the MnAs/InAs heterojunction NW is almost straight (or slightly bending) at the position of NC IV

because the tilt angle of $\langle 111 \rangle B_{IV}$ from $\langle 111 \rangle B_{IV-V}$ is approximately 7° . The height parallel to the $\langle 111 \rangle B$ directions and width of NC IV were roughly estimated to be 90 nm for the former and 100 nm for the latter from the BSE image in Figure 5-3(a). Those of NC V were approximately 105 nm for the former and 100 nm for the latter. Space separation between the NCs IV and V in the heterojunction NW was roughly estimated to be 180 nm from the BSE image. Subsequently, we conducted AFM observations of NCs IV and V to estimate their height perpendicular to the substrate surface. The inset in Figure 5-3(a) and Figures 5-3(b) to 5-3(d) show a corresponding AFM image and cross-sectional line profiles of NCs IV and V, respectively. Three white dotted lines (b) to (d) in the inset in Figure 5-3(a) represent cross-sectional planes of Figures 5-3(b) to 5-3(d), respectively. We conclude, judging from the cross-sectional line profiles of Figures 5-3(b) to 5-3(d), that the height of NC V perpendicular to the substrate surface is larger (approximately 10 nm at least) than that of NC IV. Therefore, comparing the heights of 110 to 120 nm shown in Figures 5-3(b) and 5-3(d) with the width of 100 nm obtained from the BSE image in Figure 5-3(a), it seems that the shape of cross-sectional planes (i.e., c-plane) of NC V is elliptic.

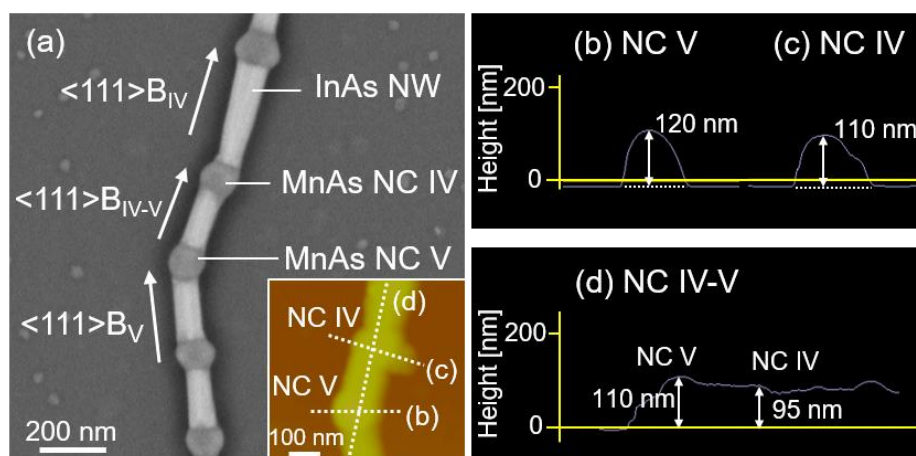


Figure 5-3. (a) A top view BSE image of a bended MnAs/InAs heterojunction NW laid on a SiO_2/Si substrate. Regions with bright and dark contrasts in the NW were due to InAs and MnAs, respectively. The $\langle 111 \rangle B$ directions of the host InAs NW were markedly tilted at the position where the MnAs NC V was formed. The inset shows a corresponding AFM image of MnAs NCs IV and V. White dotted lines in the inset represent cross-sectional planes of cross-sectional line profiles of (b) NC V, (c) NC IV, and (d) NCs IV and V (i.e., NC IV-V) observed by AFM.

Subsequently, magnetization characterizations were carried out by MFM in the PD mode for the MnAs NCs IV and V. Figures 5-4(a) to 5-4(g) show the MFM images obtained at room temperature after the applications of \mathbf{B} from 2 to 5.7 kG in the various directions shown by white thick arrows in the images. Bright and dark contrasts were obtained in the regions of NCs IV and V in the MFM images when the magnetized MFM tips detected repulsive and attractive forces from the stray magnetic fields from NCs in the heterojunction NW, respectively. The stray magnetic fields from the NCs were detected at the tip heights between 30 to 50 nm during all the MFM observations. The MFM and AFM observations using the tapping mode were carried out simultaneously in the system, i.e., the MFM observations followed the AFM observations on each of the scanning lines. According to the height values obtained by the AFM observations, the MFM tip maintained the constant tip heights from the observed objects, i.e., between 30 to 50 nm in this paper, on the heterojunction NWs or on the substrate surfaces. Therefore, in principle, the sensitivity of magnetizations could not be affected by the different heights among on MnAs NCs, on InAs NWs, and on the substrate surfaces, although the MFM tip occasionally detected the structural responses only near the edges of MnAs/InAs heterojunction NWs. To ensure that we did not detect structural responses but magnetic ones from the NCs, additional MFM observations were carried out using an MFM tip magnetized in the opposite direction. Figures 5-4(b) and 5-4(d) show the MFM images using a reversely magnetized MFM tip, i.e., the magnetized direction of the MFM tip opposite to that used in Figures 5-4(a) and 5-4(c), respectively. As shown in Figures 5-4(a) to 5-4(g), bright and dark areas were markedly observed in the NC IV and V regions. It was highly possible, as determined from the structural characterization results in Chapter 4 and magnetic characterization results for comparable samples reported in section 5.3.1, 5.3.2, and our previous study [17], that NCs IV and V had a single magnetic domain and were magnetized along one of the a -axes, i.e., the magnetic easy axes, in the current work. As shown in Figures 5-4(a), 5-4(c), 5-4(e), 5-4(f), and 5-4(g), the magnetization switching of NC IV was confirmed, i.e., the detected bright and dark contrasts were changed by the applied directions of \mathbf{B} . On the other hand, no magnetization switching was observed in NC V. Here, we should note that all the gray circles marked by M_{IV} and M_V in Figures 5-4(a) to 5-4(g) show “cross-sectional” schematic illustrations depicting the possible magnetizations, M_{IV} and M_V , which are drawn by black arrows in the gray circles, of NCs IV and V, respectively. The cross-sectional planes of the schematic illustrations were indicated by the white dotted lines in Figure 5-4(a). On the other

hand, all the MFM images were “top” views. For NC IV, the bright-dark contrast series were reversed by using a reversely magnetized MFM tip in all the observations, e.g., from Figures 5-4(a) to 5-4(b) and 5-4(c) to 5-4(d). However, for NC V, the contrasts in the images were not reversed occasionally in some of the observations, as compared in Figures 5-4(c) and 5-4(d). We obtained the same MFM images even when we changed the observation orders of NCs IV and V, i.e., whether the MFM scanning started from the NC IV (top) side or the NC V (bottom) side of the images. We confirmed from these results that no magnetization switching of the MFM tips occurred in the current work by the NCs’ magnetization during the MFM observations, which

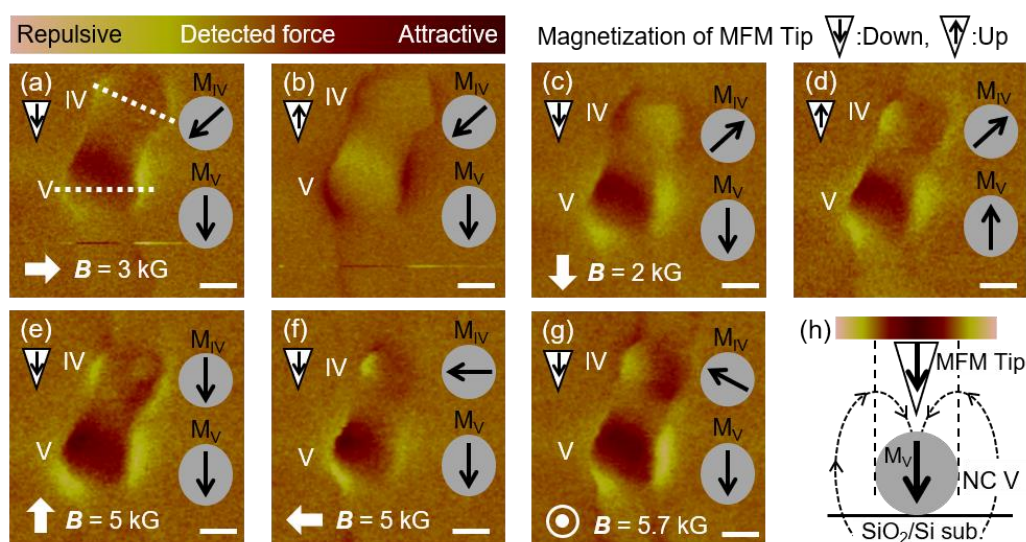


Figure 5-4. (a)-(g) Top view MFM images of MnAs NCs IV and V observed at room temperature, in which white scale bars represent 100 nm. The external magnetic fields B of 2 to 5.7 kG were applied before the MFM observations of (a), (c), (e), (f), and (g). MFM images of (b) and (d) were taken with a reversely magnetized MFM tip, i.e., the magnetized direction of the MFM tip opposite to that used in (a) and (c), respectively, to ensure that the obtained bright-dark contrast series observed in the NC IV and V regions were due to the magnetic responses from the NCs. All the gray circles marked by M_{IV} and M_V as an inset in (a)-(g) show “cross-sectional” schematic illustrations depicting the possible magnetizations, M_{IV} and M_V , which are drawn by black arrows in the gray circles, of NCs IV and V, respectively. White dotted lines in (a) indicate the cross-sectional planes of the schematic illustrations. (h) Cross-sectional illustration showing a possible magnetic response from the NC V when the NC V was magnetized along the magnetization direction of the MFM tip.

was investigated in detail in our previous study [18]. We concluded from the results in Figures 5-4(a) to 5-4(g) that all the magnetization directions of NC V were in the “downward” direction when we used an MFM tip magnetized downward, as depicted in the schematic illustration of Figure 5-4(h). Figure 5-5 shows the dependence of MFM image contrasts, in particular, in NC V, on the orders of MFM scans using a reversely magnetized MFM tip, i.e., using first the “upward” magnetization, and then, the “downward” magnetization of MFM tip (first, “upward” in Figure 5-5(a), and then, “downward” in Figure 5-5(b)) and vice versa (first, “downward” in Figure 5-5(c), and then, “upward” in Figure 5-5(d)). The observation results in Figure 5-5 were consistent

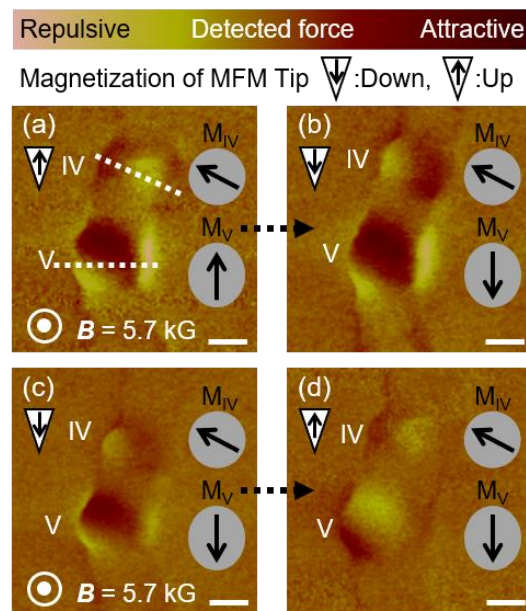


Figure 5-5. (a)-(d) Top view MFM images of NCs IV and V observed at temperature, in which white scale bars represent 100 nm. The external magnetic fields B of 5.7 kG were applied perpendicular to the SiO_2/Si substrate surface before the MFM observations of (a) and (c). Just after the MFM observations of (a) and (c), MFM images of (b) and (d) were taken in series, respectively, with a reversely magnetized MFM tip, i.e., the magnetized direction of the MFM tip opposite to that used in (a) and (c), respectively. Therefore, the serial MFM observations were carried out in the order of (a)-(b) and (c)-(d), respectively, as shown by black-dotted arrows between the images. All the gray circles in (a)-(d) show “cross-sectional” schematic illustrations depicting the possible magnetizations, M_{IV} and M_V , which are drawn by black arrows in the gray circles, of NCs IV and V, respectively. White dotted lines in (a) indicate the cross-sectional planes of the schematic illustrations.

with the results obtained in Figures 5-4(a) to 5-4(g), as depicted in Figure 5-4(h). In the case of the use of “upward” magnetization of MFM tips, the magnetization directions of NC V were occasionally changed, as compared in Figures 5-4(b), 5-4(d), 5-5(a), and 5-5(d). Judging from the detailed experimental results of magnetization switching in Figures 5-4 and 5-5, we observed no significant magnetic interaction between NCs IC and V at a relatively close range (i.e., in the estimated space separation of approximately 180 nm) in the bended heterojunction NW in the current work.

From all the observation results in this section, there seemed to be two possibilities for the results that no magnetization switching of NC V was observed by the application of \mathbf{B} : Firstly, the coercivity (or, coercive force), H_c , of NC V was so large that the magnetization switching of NC V could not occur up to \mathbf{B} smaller than 5.7 kG. Secondly, the H_c of NC V was so small that the magnetization switching of NC V could occur easily by the magnetization of MFM tips during the AFM observations using the tapping mode, in which the magnetized MFM tips tapped the MnAs NC surfaces before the MFM observations. However, the first possibility mentioned above seemed not to be practical because the bright-dark contrasts series of NC V in the images should be reversed by using a reversely magnetized MFM tip unless the magnetization switching of NC V by applying \mathbf{B} nor that of MFM tip during the observations occurred, as observed in Figure 5-4. Therefore, the second possibility was highly probable in the current work. In this case, i.e., the relatively small H_c of NC V comparing to the H_c , 950 Oe, of MFM tips, a dark region was observed at the center of the NC, and bright regions were observed around the dark region because the NC was magnetized in the same direction as the magnetization direction of MFM tips, as shown in Figure 5-4(h). Therefore, this assumption that the H_c of NC V was relatively small was consistent with the MFM observation results in Figures 5-4 and 5-5. There are some possible factors for the decrease in H_c of NC V. The bulk MnAs shows the first-order structural phase transition between the paramagnetic orthorhombic β -phase (β -MnAs, MnP-type) and the ferromagnetic hexagonal α -phase (α -MnAs, NiAs-type) at around or above room temperature. It was reported that the temperature for the phase transition, i.e., Curie temperature, T_c , was increased by applying an external tensile strain for the bulk MnAs [19]. In general, the saturation magnetization, M_s , is increased with increasing T_c . As explained in the Stoner-Wohlfarth model [20], H_c is inversely proportional to M_s , i.e., H_c is decreased with increasing M_s . This tendency

was actually observed in the papers related to other materials systems [21, 22]. In our materials system, a lattice mismatch between a c-plane of hexagonal NiAs-type MnAs and a $\{111\}$ B plane of ZB-type InAs was estimated to be approximately 13%, i.e., the lattice constant of InAs was approximately 13% larger than that of MnAs. The NC V was formed at the markedly bending position in the heterojunction NWs whereas the NC IV was at the almost straight (or slightly bending) position. It is possible that a lattice strain, i.e., a tensile strain here, exists in the MnAs NCs formed at the bending positions in the heterojunction NWs, as in the case of NC V. For the NCs formed in the straight heterojunction NWs, as in the case of NC IV, we have observed that a lattice strain is possibly accumulated in a few MnAs layers near the heterointerfaces between MnAs NCs and InAs NWs, if it exists, judging from the image contrasts observed near the heterointerfaces in cross-sectional lattice images and the electron-beam diffraction patterns of MnAs NCs reported in Chapter 4. Significant difference between NCs V and IV we markedly observed was the crystallographic directions of heterointerfaces between MnAs and InAs. The NC shape may affect a lattice strain in the MnAs NCs. The possibility that a tensile strain is one of the factors for the decrease in H_c has not been excluded thus far. The shape anisotropy of NC V is also considered as a possible factor for the decrease in H_c . The shape of c-plane, magnetic easy plane, of NC V is possibly elliptic, i.e., the NC height along the magnetization direction of the MFM tip is larger than the width, as mentioned in the end of the structural characterization part in this section. On the other hand, the c-plane of NC IV has low shape anisotropy. It is possible that NC V was easily magnetized in the same direction as the magnetization direction of the MFM tip by the shape anisotropy. The possibility of intermixture of In and Mn in the NCs is also not excluded as a factor of the decrease in H_c . It was reported that MnAs precipitates in (Ga,Mn)As thin films enhanced their H_c and, on the other hand, that H_c of (Ga,Mn)As thin films without the MnAs precipitates was decreased with increasing Mn concentration [23, 24]. For InMnAs nanodots, the H_c was decreased with increasing Mn concentration [25]. We have not observed any granular structures or precipitates in the NCs IV and V. Since the NCs IV and V had no significant difference in brightness of the BSE image of Figure 5-3(a), they possibly have similar solid compositions. Therefore, if both NCs IV and V can be grown as a single crystal InMnAs NC without MnAs precipitates, and if NC V have higher Mn contents than NC IV, it possibly leads to the decrease in H_c of NC V. However, this hypothesis is less probable because we have never observed thus far such InMnAs NCs in the other comparable heterojunction NWs by TEM

and energy dispersive X-ray spectroscopy. Since it was quite difficult to examine the same MnAs/InAs heterojunction NW observed in this paper by TEM and/or Raman spectroscopy, we have no further information of a lattice strain and solid compositions in the MnAs NCs formed at the bending positions in the heterojunction NWs. Detailed experiments and observations are required before we can conclude. But, we obtain the perspectives of controlling the H_c of NCs in the heterojunction NWs by varying the shape anisotropy of NCs or by growing InMnAs NCs. The shape anisotropy of NCs can be controlled by the growth conditions, as indicated in Chapter 4, and by the shape anisotropy in $\{111\}$ B planes of the host InAs NWs, which depends on the shape of initial circular openings in SiO₂-mask on GaAs (111)B substrates in our SA-MOVPE technique. In addition, it is possible that InMnAs NCs grow in the heterojunction NWs by supplying not only Mn source but also In (and As) source materials for the NC growth after the host InAs NW growth. The Mn content of InMnAs NCs, which affects the H_c , can be controlled by the growth conditions, such as partial pressures, temperature, and time.

5.4 Conclusions

We reported on the magnetization and magnetic domain of ferromagnetic MnAs NCs in MnAs/InAs heterojunction NWs. MnAs NCs normally have marked single magnetic domains in the heterojunction NWs. Some of the MnAs NCs were magnetized along the applied external magnetic field which was perpendicular to the $\langle 111 \rangle$ B direction of the host InAs NWs. These results are consistent with the structural characterization results in Chapter 4 because the a-axes, i.e., magnetic easy axes of the hexagonal NiAs-type MnAs, is perpendicular to the $\langle 111 \rangle$ B direction of the host InAs NWs in the MnAs/InAs heterojunction NWs. The MnAs NC with a large aspect ratio were magnetized along the c-axis, i.e., magnetic hard axis, due to the magnetic shape anisotropy along the c-axis after the application of the external magnetic field nearly parallel to the c-axis. For the MnAs NC formed at the markedly bending position in the bended heterojunction NW, the magnetization was occasionally directed by the MFM tip magnetization possibly due to its small coercivity. We believe that the MnAs NCs in heterojunction NWs, whose magnetization can be controlled by growth conditions, plays a useful role in the development of NW spintronic technologies.

Bibliography

- [1] R. Kodaira, S. Hara, K. Kabamoto, and H. Fujimagari, *Jpn. J. Appl. Phys.* **55**, 075503 (2016).
- [2] R. Kodaira, K. Kabamoto, and S. Hara, *Jpn. J. Appl. Phys.* **56**, 06GH03 (2017).
- [3] R. Kodaira, R. Horiguchi, and S. Hara, *J. Cryst. Growth* **507**, 241 (2019).
- [4] N. P. Dasgupta, J. Sun, C. Liu, S. Brittman, S. C. Andrews, J. Lim, H. Gao, R. Yan, P. Yang, *Adv. Mater.* **26**, 2137 (2014).
- [5] J. Wallentin, N. Anttu, D. Asoli, M. Huffman, I. Åberg, M. H. Magnusson, G. Siefert, P. Fuss-Kailuweit, F. Dimroth, B. Witzigmann, H. Q. Xu, L. Samuelson, K. Deppert, M. T. Borgström, *Science* **339**, 1057 (2013).
- [6] T. Tanaka, K. Tomioka, S. Hara, J. Motohisa, E. Sano, T. Fukui, Vertical surrounding gate transistors using single InAs nanowires grown on si substrates, *Appl. Phys. Express* **3**, 025003 (2010).
- [7] N. Han, F. Wang, J. J. Hou, S. P. Yip, H. Lin, F. Xiu, M. Fang, Z. Yang, X. Shi, G. Dong, T. F. Hung, J. C. Ho, *Adv. Mater.* **25**, 4445 (2013).
- [8] P. Offermans, M. Crego-Calama, S. H. Brongersma, *Nano Lett.* **10**, 2412 (2010).
- [9] J. Hubmann, B. Bauer, H. S. Körner, S. Furthmeier, M. Buchner, G. Bayreuther, F. Dirnberger, D. Schuh, C. H. Back, J. Zweck, E. Reiger, D. Bougeard, *Nano Lett.* **16**, 900 (2016).
- [10] M. Tanaka, S. Ohya, P. N. Hai, *Appl. Phys. Rev.* **1**, 011102 (2014).
- [11] M. T. Elm and S. Hara, *Adv. Mater.* **26**, 8079 (2014).
- [12] S. Sugahara and J. Nitta, *Proc. IEEE* **98**, 2124 (2010).
- [13] D. G. Ramlan, S. J. May, J. G. Zheng, J. E. Allen, B. W. Wessels, and L. J. Lauhon, *Nano Lett.* **6**, 50 (2006).
- [14] S. Hara and T. Fukui, *Appl. Phys. Lett.* **89**, 113111 (2006).
- [15] M. T. Elm, C. Michel, J. Stehr, D. M. Hofmann, P. J. Klar, S. Ito, S. Hara, and H.-A. Krug von Nidda, *J. Appl. Phys.* **107**, 013701 (2010).
- [16] E. Sánchez, M. T. Deluigi, G. Castellano, *Microsc. Microanal.* **18**, 1355 (2012).
- [17] K. Kabamoto, R. Kodaira, and S. Hara, *J. Cryst. Growth* **464**, 80 (2017).
- [18] R. Horiguchi, H. Kato, K. Kabamoto, R. Kodaira, S. Hara, *Jpn. J. Appl. Phys.* **56**, 06GH05 (2017).
- [19] F. Iikawa, M. J. S. P. Brasil, C. Adriano, O. D. D. Couto, C. Giles, P. V. Santos, L. Däweritz, I. Rungger, S. Sanvito, *Phys. Rev. Lett.* **95**, 077203 (2005).

- [20] E. C. Stoner and E. P. Wohlfarth, *Philos. Trans. R. Soc. Lond., Ser. A* **240**, 599 (1948).
- [21] S. J. Potashnik, K. C. Ku, R. F. Wang, M. B. Stone, N. Samarth, P. Schiffer, S. H. Chun, *J. Appl. Phys.* **93**, 6784 (2003).
- [22] Q. Gan, R. A. Rao, C. B. Eom, J. L. Garrett, M. Lee, *Appl. Phys. Lett.* **72**, 978 (1998).
- [23] K. Y. Wang, M. Sawicki, K. W. Edmonds, R. P. Campion, A. W. Rushforth, A. A. Freeman, C. T. Foxon, B. L. Gallagher, T. Dietl, *Appl. Phys. Lett.* **88**, 022510 (2006).
- [24] M. Sawicki, K. Y. Wang, K. W. Edmonds, R. P. Campion, A. W. Rushforth, C. T. Foxon, B. L. Gallagher, T. Dietl, *J. Magn. Magn. Mater.* **310**, 2126 (2007).
- [25] J. Novák, A. Dujavová, I. Vávra, S. Hasenöhrl, M. Reiffers, *J. Magn. Magn. Mater.* **327**, 20 (2013).

Chapter 6

Magnetotransport Characterization of Single Nanowires

We report on the magnetotransport properties of single undoped-InAs and MnAs/InAs heterojunction nanowires grown by combining the catalyst-free selective-area metal-organic vapor phase epitaxy of InAs nanowires and the endotaxial nanoclustering of MnAs. The single InAs nanowires show universal conductance fluctuations, a negative magnetoresistance due to the suppression of weak localization at low temperature as well as an ordinary positive magnetoresistance. In contrast, MnAs/InAs heterojunction nanowires show a linear negative magnetoresistance owing to the formation of magnetic polarons in the host InAs nanowires. The magnetic polarons of the host InAs nanowires are probably caused by Mn-doping and/or thermal diffusion of Mn atoms from the MnAs nanoclusters during the endotaxial growth of MnAs nanoclusters.

6.1 Introduction

The integration of vertical free-standing nanowires (NWs), which have tremendous potential for applications in next-generation electronic, photonic, biochemical sensing, and even spintronic devices, is currently of great interest [1-6]. For example, practical ways of installing vertical surrounding gate field-effect transistors (FETs) using NWs for current integrated circuits based on CMOS technologies have been demonstrated [7]. In recent semiconductor nanospintronics research fields, on the other hand, heteroepitaxial structures of ferromagnetic and III-V compound semiconductors have attracted much attention because of possible additional functionalities provided for current semiconducting devices and integrated circuits. Among them, granular hybrid structures containing ferromagnetic nanoclusters (NCs) embedded into semiconductor

layers are one of the most attractive candidates for future nanospintronic devices, because they exhibit huge magnetoresistance (MR) effects, a relatively long spin-relaxation time, and interesting magnetotransport properties [8-11]. As described in the previous chapter, we have developed a hybridization technique for the growth of ferromagnetic MnAs NCs and vertical free-standing semiconducting InAs NW templates by catalyst-free selective-area metal-organic vapor phase epitaxy (SA-MOVPE) method in order to create novel magneto-nanoelectronic or nanospintronic devices, such as vertical spin-NW-transistors. To create devices using vertical free-standing semiconducting NW channels with our surrounding gate structures [3, 12], it is crucial to investigate transport properties of our NWs. Therefore, in this chapter, we report on the magnetotransport properties of our single undoped-InAs and MnAs/InAs heterojunction NWs.

6.2 Experimental procedure

We fabricated two types of vertical free-standing NWs, i.e., InAs and MnAs/InAs heterojunction NWs, on GaAs (111)B substrates by utilizing the SA-MOVPE process for InAs NW growth and the endotaxy of MnAs in InAs for the MnAs NC growth. The fabrication process for these NWs was mostly similar to that explained in chapter 4 and our previous study [13]. For the InAs NWs, the growth temperature and growth time were 560 °C and 30 min, respectively. On the other hand, for the MnAs/InAs heterojunction NWs, the host InAs NW templates were grown at 580 °C for 30 min, and MnAs NCs were grown at 580 °C for 1 min. For the magnetotransport measurements of single NWs, the vertical InAs and MnAs/InAs heterojunction NWs were detached from the GaAs (111)B substrates mechanically by ultrasonic vibration in isopropanol solution, and deposited on SiO₂/Si substrates. Electrical contacts for two-terminal measurements were prepared on single NWs using electron-beam lithography followed by thermal evaporation of Ti/Au or Ti/Pd/Au thin layers. We fabricated three types of single NW samples in this study as listed in Table 1. Ti/Au (20 nm/200 nm), Ti/Au (20 nm/180 nm), and Ti/Pd/Au (20 nm/20 nm/60 nm) were used as electrical contacts for the samples NW15C, NW34B, and NW01B, respectively. Just before the metal evaporation, the electrical contact areas of NW15C and NW34B were treated with Semico Crean 23 solution and argon milling, respectively, to etch off the native oxide on the NW surface. The temperature dependence of the resistance as well as the MR was investigated at temperatures below 280 K using an Oxford VTI-cryostat. The sample was cooled with liquid

helium, embedded in a superconducting magnet system yielding external magnetic fields up to 10 T. The activation energies E_A were roughly estimated from the results of the temperature-dependent measurements of the resistance in a temperature range from 200 to 280 K. The properties of each samples such as the NW length L between the electrical contacts, the NW diameter d and E_A are summarized in Table 6-1. Structural characterizations to estimate the L and d were carried out by scanning electron microscopy (SEM) using a Hitachi SU8010.

Table 6-1. Properties of the different single NW samples investigated in this study. The NW length L between electrical contacts and the NW diameter d are roughly estimated from top view SEM images. The resistance R at 280 K and the activation energies E_A are taken from the results of the temperature dependent measurements.

Sample Name	Materials	L [μm]	d [nm]	R at 280 K [Ω]	E_A [meV]
NW15C	InAs	8.3	200	1.2×10^5	14
NW34B	InAs	1.9	70-90	9.0×10^5	105
NW01B	MnAs/InAs	3.4	200-250	3.0×10^9	7

6.3 Results and discussion

6.3.1 Magnetotransport properties of single InAs nanowires

First, temperature dependent resistance measurements without any application of an external magnetic field were conducted for the samples NW15C and 34B. Figures 6-1(a) and 6-1(b) show the temperature dependent resistance of NW15C and NW 34B, respectively. The insets show top view SEM images of each sample. As shown in Figures 6-1(a) and 6-1(b), both samples NW15C and NW34B show the typical semiconducting behavior with a decreasing resistance R with increasing temperature T . However, a markedly higher R and E_A of NW34B is observed compared to that of NW15C. It seems that a large contact resistance in two-terminal measurements for NW34B is the main reason for the high R and E_A , as different surface treatment methods were used to etch off the native oxide for NW15C and NW34B.

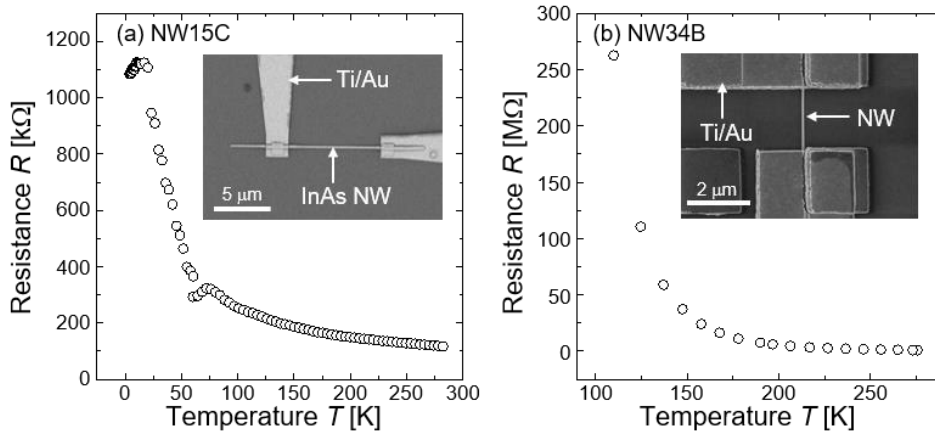


Figure 6-1. Temperature dependence of the resistance R of the single NW samples (a) NW15C and (b) NW34B. The insets in (a) and (b) show top view SEM images of NW15C and NW34B, respectively. The activation energies E_A are roughly estimated in the temperature range from 200 to 280 K. A larger R and E_A of NW34B compared to that of NW15C possibly arises from a larger contact resistance in the two-terminal measurements, caused by different surface treatments used to etch off the native oxide at the contact areas.

Subsequently, magnetotransport measurements were performed for the sample NW15C. Figure 6-2(a) shows the temperature dependence of the magnetoresistance (MR) of NW15C. The MR is defined as $MR = [R(\mathbf{B}, T) - R(0, T)] / [R(0, T)]$, where $R(\mathbf{B}, T)$ is the resistance R at an external magnetic field \mathbf{B} and at a temperature T . \mathbf{B} was applied from 0 to 10 T perpendicular to the InAs NW axis as shown in the inset of Figure 6-2(a). We observe an ordinary positive MR at all of temperatures, which is caused by the deflection of the charge carriers due to the Lorentz-force when a magnetic field \mathbf{B} is applied. In addition, a negative MR and universal conductance fluctuations (UCFs) are observed at lower temperatures in the magnetic field range from 0 to 3 T, as shown in Figure 6-2(b). UCFs of InAs NWs at low temperature, which indicate electron phase coherence transport, are also reported elsewhere [14, 15]. The negative MR at low temperature arises due to the suppression of the weak localization (WL) by applying \mathbf{B} . Although weak antilocalization (WAL), leading to positive MR, is generally observed in materials with strong spin-orbit interaction such as InAs, there are also reports of WL in InAs NWs [14, 16, 17]. It was reported that both WAL and WL are observed in the same InAs NW and that a crossover from

WAL to WL occurs as the carrier concentration is decreased by applying a gate voltage. Thus, the negative MR of NW15C caused by WL indicates a low carrier concentration in the NW due to the carrier compensation by unintentional Mn doping. In general, InAs grown without any intentional doping shows an n-type behavior mainly due to carbon impurities incorporated from the organometallic sources used for the growth, which act as donor in InAs [18]. In our previous study [3], InAs NWs also showed an n-type behavior similar to other reported InAs NWs [14, 19-21]. On the other hand, MnAs NCs formed on GaInAs/InP layers [22] and hybrid GaAs NW with MnAs NCs [23] showed a p-type behavior due to thermal diffusion of Mn atoms into the host matrix during the endotaxial growth of MnAs NCs, where Mn act as an acceptor. The InAs NWs observed in this study were grown in the same reactor, where the Mn source had been supplied for the MnAs NCs growth before. Therefore, it is possible that a carrier compensation in InAs NWs occurred due to slightly unintentional Mn doping. In addition, the carrier compensation may also be responsible for the higher R of our NW samples. The presence of a WL effect indicates that the spin relaxation length is longer or equal in magnitude to the phase coherence length [14, 16, 17]. Furthermore, $\langle 111 \rangle$ -B-oriented InAs NW channels are a promising materials system in terms of enhanced spin lifetime [24]. Thus, our results suggest the potential application of our InAs NWs for nanospintronic devices requiring long spin coherence length.

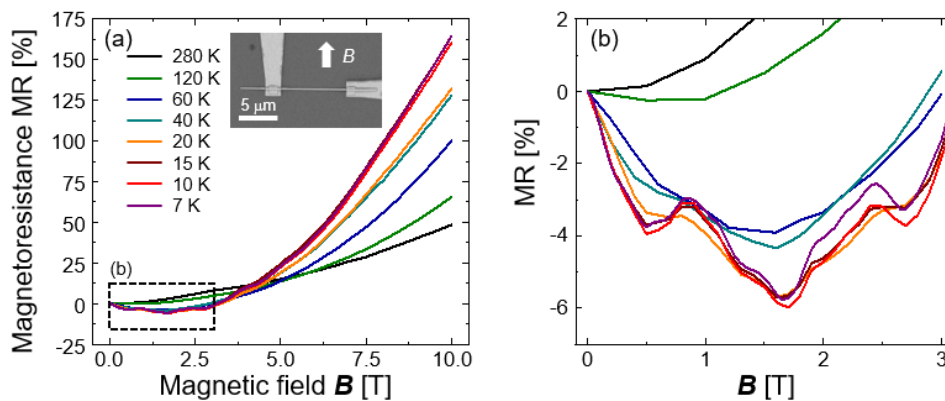


Figure 6-2. (a) Temperature dependence of the magnetoresistance (MR) of NW15C. The MR is defined as $MR = [R(\mathbf{B}, T) - R(0, T)]/[R(0, T)]$, where $R(\mathbf{B}, T)$ is the resistance R at an external magnetic field \mathbf{B} and at a temperature T . \mathbf{B} was applied from 0 to 10 T perpendicular to the InAs NW axis as represented by the white thick arrow in the inset of (a). (b) Magnification of (a) in the magnetic field range from 0 to 3 T. Universal conductance fluctuations and a negative MR due to weak localization are observed at lower T .

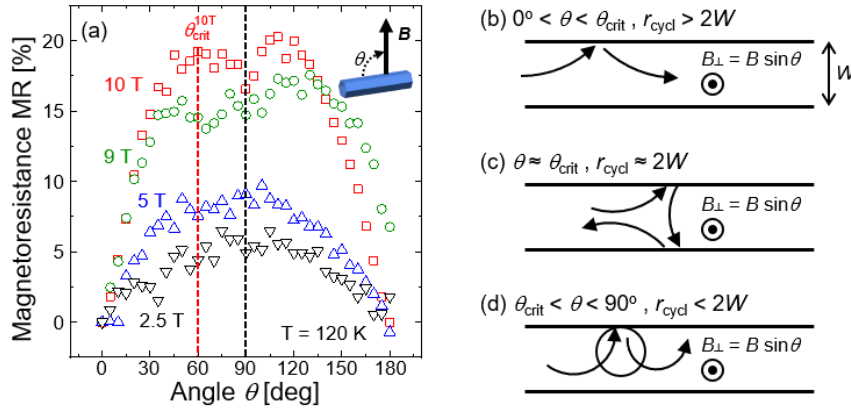


Figure 6-3. (a) Angle dependence of the magnetoresistance (MR) of NW34B at 120 K for different external magnetic fields \mathbf{B} . The angle-dependent MR is defined as $MR = [R(\theta) - R(0)]/[R(0)]$, where $R(\theta)$ is the resistance R at an angle θ between \mathbf{B} and the NW axis as schematically illustrated in the inset. The maximum MR at $\mathbf{B} = 10$ T is observed at θ_{crit} of approximately 60° . (b)-(d) Schematic illustrations of the electron trajectories, indicated by black arrows, with an additional diffusive boundary scattering contribution in the channel width W . The radius of the cyclotron orbits r_{cycl} decreases with increasing θ . (c) When $r_{\text{cycl}} \approx 2W$, the maximum backscattering led to a maximum in R and the MR [25].

Figure 6-3(a) shows the angle-dependent MR of NW34B at 120 K for different external magnetic fields \mathbf{B} . The magnetic field strength B was varied from 2.5 to 10 T in this study. The angle-dependent MR is defined as $MR = [R(\theta) - R(0)]/[R(0)]$, where $R(\theta)$ is the resistance R at an angle θ between \mathbf{B} and the NW axis, as schematically illustrated in Figure 6-3(a), i.e., θ is 90° when \mathbf{B} is applied perpendicular to the NW axis. In principle, the largest (smallest) MR is observed when \mathbf{B} is applied perpendicular (parallel) to the NW axis as the magnetic field forces the electrons on circular trajectories due to the Lorentz force resulting in additional scattering, as shown in the MR measurement results for $\mathbf{B} = 2.5$ and 5 T. However, for larger $\mathbf{B} = 9$ and 10 T, a maximum MR is observed at a critical angle θ_{crit} lower than 90° , for example, θ_{crit} is approximately 60° for 10 T. The maximum MR indicate an additional backscattering contribution caused by diffuse boundary scattering [25]. When \mathbf{B} is applied with an angle θ between 0° and θ_{crit} , the electrons which are forced on circular trajectories by the Lorentz force are additionally scattered at the NW boundaries resulting in an additional boundary scattering contribution and thus in a

higher resistance. With increasing θ the radius of the circular trajectories r_{cycl} decreases as r_{cycl} is inversely proportional to $B\sin\theta$. As shown schematically in the illustration of Figure 6-3(b), which shows an example of the electron trajectories in the channel width W , the smaller electron circuits result in an increased backscattering contribution to the resistance. When r_{cycl} reaches $2W$ at θ_{crit} , the maximum backscattering led to a maximum MR [25] as schematically illustrated in Figure 6-3(c). For larger angles θ ranging from θ_{crit} to 90° , the r_{cycl} becomes smaller than $2W$ as shown in Figure 6-3(d), resulting in a suppression of the boundary backscattering contribution and in a decrease in MR. Therefore, the maximum MR is observed at θ_{crit} lower than 90° for large $B = 9$ and 10 T. On the other hand, for $B = 2.5$ and 5 T, the magnetic field strength is not sufficient to force the electrons on trajectories with r_{cycl} smaller than $2W$, which led to a large backscattering contribution in the whole range of θ . Therefore, it is highly possible that the maximum MR appears at almost 90° for $B = 2.5$ and 5 T as shown in Figure 6-3.

6.3.2 Magnetotransport properties of single MnAs/InAs nanowires

Finally, magnetotransport measurements were conducted for a single MnAs/InAs heterojunction NW of the sample NW01B. Figure 6-4(a) shows a top view SEM image of NW01B, which has at least two MnAs NCs located between the electrical contacts as marked by white circles. Figure 6-4(b) shows the temperature-dependent MR of NW01B. The MR is defined as $\text{MR} = [R(\mathbf{B}, T) - R(0, T)]/[R(0, T)]$, as well as the case of NW15C. The external magnetic field \mathbf{B} is applied from -10 to 10 T perpendicular to the NW axis as shown in Figure 6-4(a). The NW01B shows a linear negative MR at temperatures below 20 K in contrast to the single undoped-InAs NW samples NW15C and NW34B. Similar characteristic transport properties were reported for Mn-implanted GaAs NWs [26]. The negative MR is associated with spin-dependent hopping transport, which was explained by a theoretical model of magnetic polarons [27]. The magnetic polarons are formed by exchange interaction between localized holes and magnetic impurities due to the implanted Mn atoms. By applying \mathbf{B} the magnetic moments of the polarons are aligned, which enhances spin-dependent hopping between the polarons, leading to a decrease in R and a negative MR. On the other hand, an increase in temperature causes the randomization of the orientation of the magnetic moments of the polarons, leading to a smaller negative MR effect.

Thus, the negative MR effect becomes smaller with increasing temperature, and consequently, no marked MR is observed at 40 K as shown in Figure 6-4(b). Thus, the negative MR effect strongly supports the assumption of non-intentional Mn-doping and/or thermal diffusion of Mn atoms from MnAs NCs during the endotaxial growth of MnAs NCs in our MnAs/InAs heterojunction NWs.

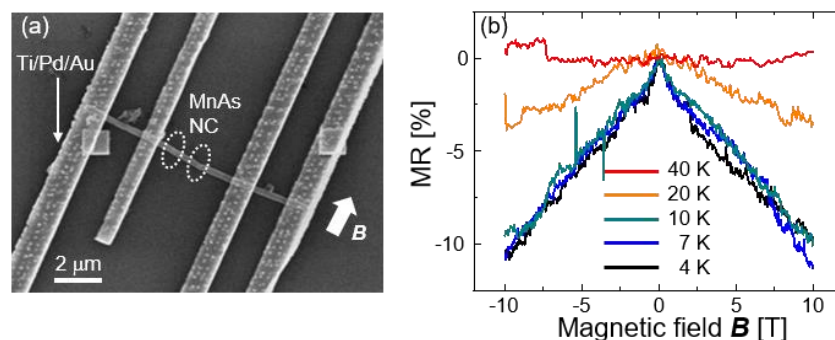


Figure 6-4. (a) A top view SEM image of NW01B, which has at least two MnAs NCs between the electrical contacts as marked by white circles. (b) Temperature dependence of the magnetoresistance (MR) of NW01B. The MR is defined as $MR = [R(\mathbf{B}, T) - R(0, T)] / [R(0, T)]$, where $R(\mathbf{B}, T)$ is the resistance R at an external magnetic field \mathbf{B} and at a temperature T . \mathbf{B} was applied from 0 to 10 T perpendicular to the NW axis as represented by the white thick arrow in (a). The linear negative MR at low T indicated the formation of magnetic polarons [26, 27] by Mn-atoms in the host NW, due to non-intentional doping and/or thermal diffusion of Mn atoms from MnAs NCs during the endotaxial growth of MnAs NCs.

6.4 Conclusions

We demonstrated the magnetotransport properties of single undoped-InAs and MnAs/InAs heterojunction NWs. In the temperature-dependent magnetoresistance (MR) measurements for the single InAs NW, universal conductance fluctuations and a negative MR effect are observed at low temperature as well as an ordinary positive MR. The negative MR is due to the suppression of weak localization by applying an external magnetic field. The angle-dependent MR measurement results of the single InAs NW indicate an additional backscattering contribution

caused by diffusive boundary scattering which depends on the transport channel width and the radius of the electron cyclotron orbits, which are caused by the Lorentz force in the presence of an external magnetic field. The MnAs/InAs heterojunction NW shows a negative MR in contrast to the single InAs NWs. These results suggest that magnetic polarons are formed in the host InAs NWs due to non-intentional Mn-doping and/or thermal diffusion of Mn atoms from MnAs NCs during the endotaxial MnAs NC growth.

Bibliography

- [1] N. P. Dasgupta, J. Sun, C. Liu, S. Brittman, S. C. Andrews, J. Lim, H. Gao, R. Yan, P. Yang, *Adv. Mater.* **26**, 2137 (2014).
- [2] J. Wallentin, N. Anttu, D. Asoli, M. Huffman, I. Åberg, M. H. Magnusson, G. Siefert, P. Fuss-Kailuweit, F. Dimroth, B. Witzigmann, H. Q. Xu, L. Samuelson, K. Deppert, M. T. Borgström, *Science* **339**, 1057 (2013).
- [3] T. Tanaka, K. Tomioka, S. Hara, J. Motohisa, E. Sano, T. Fukui, *Appl. Phys. Express* **3**, 025003 (2010).
- [4] N. Han, F. Wang, J. J. Hou, S. P. Yip, H. Lin, F. Xiu, M. Fang, Z. Yang, X. Shi, G. Dong, T. F. Hung, J. C. Ho, *Adv. Mater.* **25**, 4445 (2013).
- [5] P. Offermans, M. Crego-Calama, S. H. Brongersma, *Nano Lett.* **10**, 2412 (2010).
- [6] J. Hubmann, B. Bauer, H. S. Körner, S. Furthmeier, M. Buchner, G. Bayreuther, F. Dirnberger, D. Schuh, C. H. Back, J. Zweck, E. Reiger, D. Bougeard, *Nano Lett.* **16**, 900 (2016).
- [7] T. H. Bao, D. Yakimets, J. Ryckaert, I. Ciofi, R. Baert, A. Veloso, J. Boemmels, N. Collaert, P. Roussel, S. Demuyne, P. Raghavan, A. Mercha, Z. Tokei, D. Verkest, A. V.-Y. Thean, and P. Wambacq, *Proc. 44th European Solid-State Device Research Conf. (ESSDERC 2014)*, 2014, p. 102.
- [8] P. N. Hai, S. Ohya, M. Tanaka, S. E. Barnes, and S. Maekawa, *Nature* **458**, 489 (2009).
- [9] P. N. Hai, S. Ohya, and M. Tanaka, *Nat. Nanotechnology* **5**, 593 (2010).
- [10] M. Tanaka, S. Ohya, and P. N. Hai, *Appl. Phys. Rev.* **1**, 011102 (2014).
- [11] M. T. Elm and S. Hara, *Adv. Mater.* **26**, 8079 (2014).
- [12] Y. Kobayashi, Y. Kohashi, S. Hara, and J. Motohisa, *Appl. Phys. Express* **6**, 045001 (2013).
- [13] R. Kodaira, S. Hara, K. Kabamoto, and H. Fujimagari, *Jpn. J. Appl. Phys.* **55**, 075503 (2016).
- [14] A. E. Hansen, M. T. Björk, C. Fasth, C. Thelander, and L. Samuelson, *Phys. Rev. B* **71**, 025328 (2005).
- [15] Ch. Blömers, M. I. Lepsa, M. Luysberg, D. Grützmacher, H. Lüth, and Th. Schäpers, *Nano Lett.* **11**, 3550 (2011).
- [16] S. Dhara, H. S. Solanki, V. Singh, A. Narayanan, P. Chaudhari, M. Gokhale, A. Bhattacharya, and M. M. Deshmukh, *Phys. Rev. B* **79**, 121311 (2009).
- [17] D. Liang, M. R. Sakr, and X. P. A. Gao, *Nano Lett.* **9**, 1709 (2009).
- [18] M. Kamp, R. Contini, K. Werner, H. Heinecke, M. Weyers, H. Lüth, and P. Balk, *J. Cryst.*

-
- Growth **95**, 154 (1989).
- [19] B. J. Ohlsson, M. T. Björk, A. I. Persson, C. Thelander, L. R. Wallenberg, M. H. Magnusson, K. Deppert, L. Samuelson, *Physica E* **13**, 1126 (2002).
- [20] T. Bryllert, L. Wernersson, T. Löwgren, and L. Samuelson, *Nanotechnology* **17**, S227 (2006).
- [21] C. Rehnstedt, T. Mårtensson, C. Thelander, L. Samuelson, and L. Wernersson, *IEEE Trans. Electron Devices* **55**, 3037 (2008).
- [22] M. T. Elm, C. Michel, J. Stehr, D. M. Hofmann, P. J. Klar, S. Ito, S. Hara, and H.-A. Krug von Nidda, *J. Appl. Phys.* **107**, 013701 (2010).
- [23] S. Hara, S. Sakita, and M. Yatago, *Jpn. J. Appl. Phys.* **51**, 11PE01 (2012).
- [24] K. Biermann, A. Hernández-Mínguez, R. Hey, and P. V. Santos, *J. Appl. Phys.* **112**, 083913 (2012).
- [25] C. W. J. Beenakker and H. van Houten, *Solid State Physics* **44**, 1 (1991).
- [26] S. Kumar, W. Paschoal, Jr., A. Johannes, D. Jacobsson, C. Borschel, A. Pertsova, C.-H. Wang, M.-K. Wu, C. M. Canali, C. Ronning, L. Samuelson, and H. Pettersson, *Nano Lett.* **13**, 5079 (2013).
- [27] A. Kaminski and S. D. Sarma, *Phys. Rev. Lett.* **88**, 247202 (2002).

Chapter 7

Conclusions

In this study, synthesis of vertical ferromagnetic MnAs/semiconducting InAs heterojunction nanowires (NWs) by combining the catalyst-free selective-area metal-organic vapor phase epitaxy (SA-MOVPE) of InAs NWs and the endotaxial nanoclustering of MnAs are demonstrated. A possible growth mechanism of MnAs nanoclusters (NCs) in the vertical MnAs/InAs heterojunction NWs is discussed on the basis of the detailed crystal structural characterization and the growth condition dependence results. In addition, we also report on their magnetization and magnetotransport characterizations results. We believe that our vertical MnAs/InAs heterojunction NWs in the current work have demonstrated new possibilities and versatility in the creation of future novel nanospinronic NW devices using vertical semiconducting NWs with vertical surrounding gate structures. Summary and conclusions are the following.

In chapter 4, we reported on the synthesis and structural characterizations of vertical MnAs/InAs heterojunction NWs by combining the SA-MOVPE of InAs NWs and the endotaxial nanoclustering of MnAs NCs. The *c*-axes, i.e., the $\langle 0001 \rangle$ directions, of the hexagonal NiAs-type MnAs NCs were approximately parallel to the $\langle 111 \rangle_B$ directions of the host zinc-blende-type (ZB-type) InAs NWs in the heterojunction NWs with the atomically abrupt complete heterointerfaces. The detailed growth condition dependences revealed that the parameters of the growth temperature T_g and the distance between NWs, or the period a , are the key factors for the formation of MnAs NCs into InAs NWs. The diffusion coefficients of manganese atoms D the surface migration length of manganese adatoms on the host InAs NWs, and the desorption rates of indium and arsenic atoms in the NWs strongly depended on the growth temperature T_g . On the other hand, NW height changed according to the period of the host InAs NWs, a . At a relatively low T_g of 490 °C, the D , surface migration length, and desorption rate decreased. This led to a relatively large number of small MnAs NCs, which were shallowly formed into the host InAs

NWs from the {0-11} sidewalls. When T_g increased, on the other hand, the D , surface migration length, and desorption rate increased. This resulted in relatively large NCs that formed deeply into the host NWs and the decrease in the number of NCs. At a T_g of 580 °C, the MnAs NCs penetrated the host InAs NWs. This phenomenon successfully led to the formation of vertical MnAs/InAs heterojunction NWs with atomically abrupt heterointerfaces between MnAs and InAs layers. The results of growth time t dependence also successfully supported the possible growth mechanism, which suggested that the arsenic atoms in the host InAs NWs were consumed for the MnAs NC formation. The size of MnAs NCs increased with increasing t of MnAs NCs. In addition, the upper part of the host InAs NWs tended to be thinner and shorter compared to the lower part ones with increasing t . Therefore, it would be possible to control the size and shape of MnAs NCs in vertical MnAs/InAs heterojunction NWs by changing the parameter t as well as T_g .

In chapter 5, we reported on the magnetization and magnetic domain of ferromagnetic MnAs NCs in MnAs/InAs heterojunction NWs. MnAs NCs normally have marked single magnetic domains in the heterojunction NWs. Some of the MnAs NCs were magnetized along the applied external magnetic field which was perpendicular to the $\langle 111 \rangle_B$ direction of the host InAs NWs. These results are consistent with the structural characterization results in Chapter 4 because the a -axes, i.e., magnetic easy axes of the hexagonal NiAs-type MnAs, is perpendicular to the $\langle 111 \rangle_B$ direction of the host ZB-type InAs NWs in the MnAs/InAs heterojunction NWs. The MnAs NC with a large aspect ratio were magnetized along the c -axis, i.e., magnetic hard axis, due to the magnetic shape anisotropy along the c -axis after the application of the external magnetic field nearly parallel to the c -axis. For the MnAs NC formed at the markedly bending position in the bended heterojunction NW, the magnetization was occasionally directed by the MFM tip magnetization possibly due to its small coercivity. We believe that the MnAs NCs in heterojunction NWs, whose magnetization can be controlled by growth conditions, plays a useful role in the development of NW spintronic technologies.

In chapter 6, we demonstrated the magnetotransport properties of single undoped-InAs and MnAs/InAs heterojunction NWs. In the temperature-dependent magnetoresistance (MR)

measurements for single InAs NWs, universal conductance fluctuations and a negative MR effect are observed at low temperature as well as an ordinary positive MR. The negative MR is due to the suppression of weak localization by applying an external magnetic field. The angle-dependent MR measurement results of single InAs NW indicate an additional backscattering contribution caused by diffusive boundary scattering which depends on the transport channel width and the radius of the electron cyclotron orbits, which are caused by the Lorentz force in the presence of an external magnetic field. The MnAs/InAs heterojunction NW show a negative MR in contrast to the single InAs NWs. These results suggest that magnetic polarons are formed in the host InAs NWs due to non-intentional Mn-doping and/or thermal diffusion of Mn atoms from MnAs NCs during the endotaxial MnAs NC growth.

List of Publications/Conferences/Awards

1. Publication related to this work

- [1] R. Kodaira, S. Hara, K. Kabamoto, and H. Fujimagari, “Synthesis and Structural Characterization of Vertical Ferromagnetic MnAs/Semiconducting InAs Heterojunction Nanowires”, Japanese Journal of Applied Physics, Vol. 55, No. 7, pp. 075503-1-075503-8 (2016). (IF=1.452, TC=3)
- [2] R. Kodaira, K. Kabamoto, and S. Hara, “Shape Control of Ferromagnetic MnAs Nanoclusters Exhibiting Magnetization Switching in Vertical MnAs/InAs Heterojunction Nanowires”, Japanese Journal of Applied Physics, Vol. 56, No. 6S1, pp. 06GH03-1-06GH03-6 (2017). (IF=1.452, TC=1)
- [3] R. Kodaira, R. Horiguchi, and S. Hara, “Magnetization characterization of MnAs nanoclusters at close range in bended MnAs/InAs heterojunction nanowires”, Journal of Crystal Growth, Vol. 507, pp. 241-245 (2019). (IF=1.742)

2. Publication relate to other works

- [1] K. Kabamoto, R. Kodaira, and S. Hara, “Magnetization in Vertical MnAs/InAs Heterojunction Nanowires”, Journal of Crystal Growth, Vol. 464, pp. 80-85 (2017).
- [2] R. Horiguchi, H. Kato, K. Kabamoto, R. Kodaira, and S. Hara, “Analyses of magnetization switching and magnetic domains in lateral MnAs nanowires in combination with structural characterization”, Japanese Journal of Applied Physics, Vol. 56, No. 6S1, pp. 06GH05-1-06GH05-6 (2017).

3. Presentations related to this work

International conference

- [1] R. Kodaira, H. Fujimagari, H. Kato, S. Sakita, and S. Hara: “Selective-Area Metal-Organic Vapor Phase Epitaxy of Hetero-Junction Nanowires between Ferromagnetic MnAs and Semiconducting InAs”, the 27th International Microprocesses and Nanotechnology Conference (MNC 2014), Fukuoka, Japan, November 4-7, 2014, 6B-6-3.
- [2] R. Kodaira, K. Kabamoto, S. Sakita, and S. Hara: “Structural and Magnetic Characterization of Vertical Ferromagnetic MnAs/Semiconducting InAs Heterojunction Nanowires”, 2015 International Conference on Solid State Devices and Materials (SSDM 2015), Sapporo, Japan, September 27-30, 2015, D-6-3.
- [3] R. Kodaira, K. Kabamoto, and S. Hara: “Growth Time Dependence of Ferromagnetic MnAs Nanoclusters Formation in Semiconducting InAs Nanowires”, The 18th International Conference on Metal Organic Vapor Phase Epitaxy (ICMOVPE-XVIII), San Diego, USA, July 10-15, 2016, 5A-2.3.
- [4] R. Kodaira, K. Kabamoto, and S. Hara: “Shape Control of Ferromagnetic MnAs Nanoclusters and Their Magnetization in Semiconducting InAs Nanowires”, The 29th International Microprocesses and Nanotechnology Conference (MNC 2016), Kyoto, Japan, November 8-11, 2016, 11B-10-4.
- [5] R. Kodaira, T. Kadowaki, and S. Hara: “Control of Bending Structures in MnAs/InAs Heterojunction Nanowires”, the 2017 Materials Research Society (MRS) Fall Meeting, Boston, Massachusetts, USA, November 26 - December 1, 2017, NM03.14.17.
- [6] R. Kodaira, R. Horiguchi, and S. Hara: “Magnetization Characterization of Two MnAs Nanoclusters at Close Range in MnAs/InAs Heterojunction Nanowires”, The 19th International Conference on Metalorganic Vapor Phase Epitaxy (ICMOVPE-XIX), Nara, Japan, June 3-8, 2018, 7C-3.6.

Domestic conference

- [1] 小平竜太郎, 藤曲央武, 加藤弘晃, 崎田晋哉, 原真二郎: 「MnAs/InAs ナノワイヤの作製と成長条件依存性評価」, 第 75 回応用物理学会秋季学術講演会, 札幌, 2014 年 9 月, 18a-A6-3.
- [2] 小平竜太郎, 梶本恭平, 崎田晋哉, 原真二郎: 「MnAs/InAs ダブルヘテロ接合ナノワイヤの作製と評価」, 第 76 回応用物理学会秋季学術講演会, 名古屋, 2015 年 9 月, 14p-2Q-7.
- [3] 小平竜太郎, 梶本恭平, 崎田晋哉, 原真二郎: 「MnAs/InAs ダブルヘテロ接合ナノワイヤの成長メカニズム」, 第 63 回応用物理学会春季学術講演会, 東京, 2016 年 3 月, 19p-W834-1.
- [4] 小平竜太郎, 門脇哲郎, 原真二郎: 「MnAs/InAs ダブルヘテロ接合ナノワイヤの屈曲構造評価」, 第 64 回応用物理学会春季学術講演会, 横浜, 2017 年 3 月, 15p-421-5.
- [5] 小平竜太郎, 堀口竜麻, P. Uredat, M. T. Elm, P. J. Klar, and 原真二郎: “Magnetotransport Properties of Single InAs Nanowires”, 第 78 回応用物理学会秋季学術講演会, 福岡, 2017 年 9 月, 7a-S44-6.
- [6] 小平竜太郎, 堀口竜麻, 原真二郎: 「屈曲した MnAs/InAs ヘテロ接合ナノワイヤの磁気特性および構造評価」, 第 65 回応用物理学会春季学術講演会, 東京, 2018 年 3 月, 19p-P8-1.

4. Presentations related to other work

International conference

- [1] K. Kabamoto, R. Kodaira, S. Sakita, and S. Hara: “Backscattered Electron and Magnetic Force Microscopy Analyses of MnAs/InAs Heterojunction Nanowires”, The 28th International Microprocesses and Nanotechnology Conference (MNC 2015), Toyama, Japan, November 10-13, 2015, 12C-6-5.
- [2] K. Kabamoto, R. Kodaira, and S. Hara: “Magnetic Domain Structure of MnAs/InAs Heterojunction Nanowires”, The 18th International Conference on Metal Organic Vapor Phase Epitaxy (ICMOVPE-XVIII), San Diego, USA, July 10-15, 2016, 5A-2.4.
- [3] R. Horiguchi, H. Kato, K. Kabamoto, R. Kodaira, and S. Hara: “Structural and Magnetic Domain Characterization of Lateral MnAs Nanowires”, The 29th International Microprocesses and Nanotechnology Conference (MNC 2016), Kyoto, Japan, November 8-11, 2016, 11B-10-3.
- [4] M. T. Elm, R. Kodaira, R. Horiguchi, K. Kabamoto, P. J. Klar, and S. Hara: “Structural Characterization and Magnetotransport Properties of MnAs/InAs Hybrid Nanowires Grown by Selective-Area Metal-Organic Vapor Phase Epitaxy”, 2016 Materials Research Society (MRS) Fall Meeting & Exhibit, Boston, USA, November 27 – December 2, 2016, NM1.2.02.
- [5] T. Kadowaki, R. Kodaira, and S. Hara: “Analysis of Bending Mechanism in MnAs/InAs Heterojunction Nanowires” 2017 International Conference on Solid State Devices and Materials (SSDM 2017), Sendai, Japan, September 19-22, 2017, J-6-02.
- [6] P. Uredat, M. T. Elm, R. Kodaira, R. Horiguchi, P. J. Klar, and S. Hara: “Electrical Transport Properties of Single MnAs/InAs Hybrid Nanowires Grown by Selective-Area Metal-Organic Vapor Phase Epitaxy”, 2017 Materials Research Society (MRS) Fall Meeting & Exhibit, Boston, USA, November 26 – December 1, 2017, NM03.07.06.
- [7] P. Uredat, R. Kodaira, R. Horiguchi, S. Hara, P. J. Klar, and M. T. Elm: “Determining the Carrier Mobility in Single InAs Nanowires from Magnetotransport Measurements”, 2018 International Conference on Solid State Devices and Materials (SSDM 2018), Tokyo, Japan,

September 9-13, 2018, M-6-02.

- [8] T. Kadowaki, R. Kodaira, and S. Hara: “Structural Investigation of Bended MnAs/InAs Heterojunction Nanowires” The 31st International Microprocesses and Nanotechnology Conference (MNC 2018), Sapporo, Japan, November 13-16, 2018, 16-11-115L.
- [9] Y. Kitazawa, R. Kodaira, R. Horiguchi, W. Jevasuwan, N. Fukata, and S. Hara: “Dependence of Si Nanowire Orientation on Vapor-Liquid-Solid Growth Conditions”, The 31th International Microprocesses and Nanotechnology Conference (MNC 2018), Sapporo, Japan, November 13-16, 2018, 16P-11-111L.

Domestic conference

- [1] 梶本恭平, 小平竜太郎, 崎田晋哉, 原真二郎: 「MnAs/InAs ヘテロ接合ナノワイヤの磁区構造評価」, 第 63 回応用物理学会春季学術講演会, 東京, 2016 年 3 月, 20p-P7-3.
- [2] 堀口竜麻, 加藤弘晃, 梶本恭平, 小平竜太郎, 原真二郎: 「横型 MnAs ナノワイヤの構造評価および磁区観察」, 第 77 回応用物理学会秋季学術講演会, 新潟, 2016 年 9 月, 14p-D62-8.
- [3] 梶本恭平, 小平竜太郎, 原真二郎: 「MnAs/InAs ヘテロ接合ナノワイヤの磁区制御」, 第 77 回応用物理学会秋季学術講演会, 新潟, 2016 年 9 月, 14p-D62-9.

5. Awards

- [1] 小平竜太郎, 「第 39 回 (2016 年秋季) 応用物理学会講演奨励賞」, 2015 年 11 月.
対象論文: 小平竜太郎, 梶本恭平, 崎田晋哉, 原真二郎: 「MnAs/InAs ダブルヘテロ
接合ナノワイヤの作製と評価」, 第 76 回応用物理学会秋季学術講演会.
- [2] SPOTLIGHTS: Editors' Choice from APEX and JJAP, 2016 (2016 年 JJAP 注目論文)
対象論文: R. Kodaira, S. Hara, K. Kabamoto, and H. Fujimagari, "Synthesis and Structural
Characterization of Vertical Ferromagnetic MnAs/Semiconducting InAs Heterojunction
Nanowires", Japanese Journal of Applied Physics, Vol. 55, No. 7, pp. 075503-1-075503-8
(2016).
- [3] HIGHLIGHTS: Editors' Choice from APEX and JJAP, 2016 (2016 年 JJAP 注目論文)
対象論文: R. Kodaira, S. Hara, K. Kabamoto, and H. Fujimagari, "Synthesis and Structural
Characterization of Vertical Ferromagnetic MnAs/Semiconducting InAs Heterojunction
Nanowires", Japanese Journal of Applied Physics, Vol. 55, No. 7, pp. 075503-1-075503-8
(2016).